creative commons
COMMONS DEED

저작자표시-비영리-변경금지 2.0 대한민국

이용자는 아래의 조건을 따르는 경우에 한하여 자유롭게

- 이 저작물을 복제, 배포, 전송, 전시, 공연 및 방송할 수 있습니다.

다음과 같은 조건을 따라야 합니다:

저작자표시. 귀하는 원저작자를 표시하여야 합니다.

비영리. 귀하는 이 저작물을 영리 목적으로 이용할 수 없습니다.

변경금지. 귀하는 이 저작물을 개작, 변형 또는 가공할 수 없습니다.

- 귀하는, 이 저작물의 재이용이나 배포의 경우, 이 저작물에 적용된 이용허락조건을 명확하게 나타내어야 합니다.
- 저작권자로부터 별도의 허가를 받으면 이러한 조건들은 적용되지 않습니다.

저작권법에 따른 이용자의 권리는 위의 내용에 의하여 영향을 받지 않습니다.

이것은 이용허락규약(Legal Code)을 이해하기 쉽게 요약한 것입니다.

Disclaimer

dCollection

이학박사 학위논문

Feasibility study of MRI-based synthetic CT generation for PET/MRI and MR-IGRT

PET/MRI 및 MR-IGRT를 위한 MRI 기반 합성 CT 생성의 타당성 연구

2020 년 8 월

서울대학교 대학원
의과학과

안 현 준

Thesis for the Degree of
Doctor of Philosophy in Science

Feasibility study of MRI-based synthetic CT generation for PET/MRI and MR-IGRT

PET/MRI 및 MR-IGRT를 위한 MRI 기반 합성 CT 생성의 타당성 연구

August 2020

Seoul National University Graduate School
Major in Biomedical Sciences

Hyun Joon An

PET/MRI 및 MR-IGRT를 위한 MRI 기반 합성 CT 생성의 타당성 연구

지도 교수 이 재 성

이 논문을 이학박사 학위논문으로 제출함

2020 년 5 월

서울대학교 대학원

의과학과

안 현 준

안현준의 이학박사 학위논문을 인준함

2020 년 8 월

위 원 장 _____ (인)

부위원장 _____ (인)

위 원 _____ (인)

위 원 _____ (인)

위 원 _____ (인)

Feasibility study of MRI-based synthetic CT generation for PET/MRI and MR-IGRT

Examiner Jae Sung Lee

Submitting a Ph.D. Dissertation of Public Administration
May 2020

Seoul National University Graduate School
Major in Biomedical Sciences
Hyun Joon An

Confirming the Ph.D. Dissertation written by Hyun Joon An
August 2020

Chair _____(Seal)

Vice Chair _____(Seal)

Examiner _____(Seal)

Examiner _____(Seal)

Examiner _____(Seal)

Abstract

Feasibility study of MRI-based synthetic CT generation for PET/MRI and MR-IGRT

Hyun Joon An
Major in Biomedical Sciences
Department of Biomedical Sciences
Seoul National University Graduate School

Over the past decade, the application of magnetic resonance imaging (MRI) in the field of diagnosis and treatment has increased. MRI provides higher soft-tissue contrast, especially in the brain, abdominal organ, and bone marrow without the expose of ionizing radiation. Hence, simultaneous positron emission tomography/MR (PET/MR) system and MR-image guided radiation therapy (MR-IGRT) system has recently been emerged and currently available for clinical study.

One major issue in PET/MR system is attenuation correction from MRI scans for PET quantification and a similar need for the assignment of electron densities to MRI scans for dose calculation can be found in MR-IGRT system. Because the MR signals are related to the proton density and relaxation properties of tissue, not to electron density. To overcome this problem, the method called synthetic CT (sCT), a pseudo CT derived from MR images, has been proposed. In this thesis, studies on generating synthetic CT and investigating the feasibility of using a MR-based

synthetic CT for diagnostic and radiotherapy application were presented.

Firstly, MR image-based attenuation correction (MR-AC) method using level-set segmentation for brain PET/MRI was developed. To resolve conventional inaccuracy MR-AC problem, we proposed an improved ultrashort echo time MR-AC method that was based on a multiphase level-set algorithm with main magnetic field inhomogeneity correction. We also assessed the feasibility of level-set based MR-AC method, compared with CT-AC and MR-AC provided by the manufacturer of the PET/MRI scanner.

Secondly, we proposed sCT generation from the low field MR images using 2D convolution neural network model for MR-IGRT system. This sCT images were compared to the deformed CT generated using the deformable registration being used in the current system. We assessed the feasibility of using sCT for radiation treatment planning from each of the patients with pelvic, thoraic and abdominal region through geometric and dosimetric evaluation.

Keyword : Synthetic CT, pseudo CT, PET/MRI, MR-IGRT, attenuation correction, electron density map

Student Number : 2012-30578

Table of Contents

Table of Figures

Table of Tables

Chapter 1. Introduction

1.1. Background

1.1.1. The Integration of MRI into Other Medical Devices

Magnetic resonance imaging (MRI) is one of the most prominently used medical imaging equipment for diagnostic purpose. MRI system use strong magnetic fields and radiofrequency pulse to make an image of the internal structures of the body. The signal comes primarily from the protons in fat and water molecules in the body.

The advantages of MRI over other imaging modalities include superior soft tissue contrast especially in the brain, abdominal organ, and bone marrow without the expose of ionizing radiation. MRI can also provide functional and molecular information, such as diffusion imaging, perfusion imaging, and functional MRI (1).

To take advantage of these MRI characteristics, the application of MRI into other medical equipment in the diagnostic and therapeutic field has increased rapidly in the past decade. As a result, positron emission tomography/MRI (PET/MRI) system and MR-image guided radiation therapy (MR-IGRT) system has recently been emerged and currently available for clinical study.

1.1.1.1 PET/MRI

For diagnostic purpose, PET is a molecular imaging modality that provides quantitative physiological information. Although PET is the most sensitive medical imaging device providing functional and biochemical information, it has limited spatial resolution, signal to noise ratio, and anatomical information. On the other hand, MRI offers detail anatomical information with excellent soft tissue contrast,

such as brain, head and neck, liver and pelvis. Accordingly, the combination of PET and MRI shows various possibilities as new methodology.

In addition, fully integrated PET/MRI scanners based on semi-conductor photosensors, such as avalanche photodiode and silicon photomultiplier allows the simultaneous acquisition of both image data sets, which possess several distinct advantages over the sequential scan in conventional PET/CT examination (1-5).

Simultaneous PET and MRI data acquisition has several advantages including temporal and spatial correlation of PET and MRI data. Motion correction and partial volume effect correction of the PET data can be implemented using the MRI information. Additionally, more accurate arterial input function for dynamic PET can be obtained using image-based approaches (6).

1.1.1.2 MR-IGRT

The goal of radiation therapy is to deliver radiation to the planned target volumes as precisely and accurately as possible while minimizing dose to critical normal tissues. IGRT is a method of radiation therapy that incorporates imaging techniques to ensure a precise dose delivery (7, 8).

IGRT is particularly applicable to highly conformal radiotherapy such as 3D conformal radiation therapy (3D-CRT) and intensity-modulated radiation therapy (IMRT) (9). In the treatment of high-dose, low-fractionaion therapy such as stereotactic body radiation therapy (SBRT) or stereotactic ablative radiotherapy (SABR) , IGRT is considered an essential component of the of the entire procedure (10).

Currently, imaging techniques such as mega-voltage planar imaging, kilo-voltage planar imaging, and cone-beam CT are commonly used to optimize

treatment positioning. However, all of these still have the problem of poor soft tissue contrast, and as a result, it still remains challenging to distinguish tumor from normal tissues (11, 12).

To solve this problem, MR-IGRT system has been developed and currently available (13-15). The integration of MRI into radiation treatment system provides a high tumor visibility and surrounding tissue anatomy. It also provides real-time imaging to characterize and track anatomical movements using fast sequence imaging. Respiratory gating by MRI is particularly advantageous in several aspects for high dose SBRT (16, 17). It enables motion mitigation and a reduction of planning target volume (PTV) margins and allows for an accurate dose delivery to the PTV by reducing dose exposure of organs at risk (OARs).

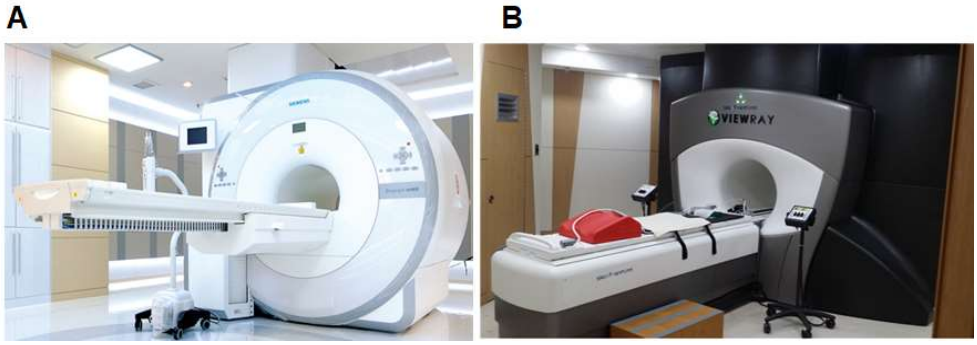

Figure 1-1. MR-integrated medical system. (A) PET/MRI : Siemens Biograph mMR (B) MR-IGRT : ViewRay MRIdian tri ^{60}Co radiotherapy system

1.1.2. Chanllenges in the MRI Integrated System

1.1.2.1 Attenuation Correction for PET/MRI

Despite the advantage of simultaneous PET/MR imaging, one of the most challenging issues in PET/MR system is attenuation correction (AC) which is an essential procedure for quantitative PET imaging. In PET/CT, the attenuation map (μ-map) can be derived from CT transmission data and converting the Hounsfield units to μ values for 511 keV using bilinear transform (18, 19). In PET/MR, there is no mechanism to directly measure the attenuation coefficient of the tissue due to space constraint and magnetic induced artifact. The MR signals are related to the proton density and relaxation properties of tissue, not to electron density. It is therefore necessary to derive μ-map from the PET or MRI data.

1.1.2.2 Electron Density for Dose Calculation of MR-IGRT

The electron density is an essential factor for accurate dose calculation. During treatment planning, the treatment planning systems (TPS) use a conversion of the Hounsfield numbers to relative electron density to calculate dose (20, 21). This can be done through use of generic formulas or tissue look up table. A look up table can help account for the effects of variations in atomic number Z between different tissues.

However, in MR-IGRT system, the MRI lack any intrinsic relationship to the electron density. As a result, additional CT simulation (CT-SIM) imaging is required to know the radiation dose distribution. In the standard MR-IGRT workflow, the CT simulation is used for dose calculation and treatment planning with daily MR images co-registered to the CT-SIM images by applying rigid or deformable registration and

assigning an electron density map obtained from the registered CT.

1.1.3. Synthetic CT Generation

In recent years, interests in deriving CT data from MRI data have grown rapidly. Several methods have been proposed for using MR images to generate a synthetic CT (sCT) image. These methods can broadly be classified into 3 groups : template(or atlas)-based, segmentation-based, and learning-based (22-24).

In template-based method, the sCT is derived by spatial transformation from a template data. The template image can be generated based on an average image from a number of CT image. The spatial transformation information is acquired from co-registered MR images (25-29). However, the use of template-based method has some limitations because the template image cannot fully accommodate the wide inter-individual anatomical variability of patient image.

In segmentation-based method, derivation of sCT is performed by MR image segmentation and assigning the attenuation coefficients to each segmented tissue voxel. For PET/MRI system, one of current clinically available segmentation based method is derived from a two-point Dixon sequence to classify soft tissue, fat tissue, lungs and background (23). But, there is no contrast difference between air and bone due to short relaxation time property of the tissues. Consequently, the bone signal is define as soft tissue in attenuation map. Substitution of bone by soft tissue in attenuation map cause the underestimation of uptake adjacent to bone regions in not only brain but also whole-body imaging. From these problems, ultra-short or zero echo time (UTE/ZTE) sequences were proposed to segment the bone tissue (30, 31). In their method, the sCT is derived from the difference between two short echo time MR images with air mask generated by region growing method. Although the results

showed that UTE sequences is feasible to generate attenuation maps, some segmentation errors occurred at the borders of the skull and complex small bone and air cavities structures.

In learning-based method, the sCT is generated by automatically machine learning the image feature relationship based on different dataset. This method, represented as the deep learning, has recently been widely used with high accuracy in brain and pelvis regions (32-36). These methods required a large number of registered CT and MRI images for training network which means feature relationships. While traning is computationally intensitve and time-consuming process, but once the initial training is completed, the prediction of sCT can be predicted in a short time. Not only is the HU value of sCT image appear very similar to the CT, but we can also train by adding a dataset for more acuurate results (37).

1.2. Purpose of Research

The aim of this thesis is to develop synthetic CT from MRI in diagnostic and therapeutic application.

In chapter 2, we proposed a MR-based attenuation correction (MR-AC) method that is based on multi-phase level set algorithm for the brain region. The algorithm automatically distinguishes three tissue components, which are air cavities, soft tissue and bone region. The accuracy of the proposed MR-AC approach was evaluated in clinical studies using simultaneously acquired brain PET/CT and PET/MR images.

In chapter 3, we proposed 2D U-net convolution neural network (CNN) to generate sCT from low magnetic field MR images for MR-IGRT. The algorithm was

applied to each of the three regions of the pelvis, thorax, and abdomen, and compared to sCT and conventional deformed CT (dCT). The feasibility of clinical use of sCT was evaluated through quantitative analysis through geometrical and dosemetrical evaluation.

Chapter 2. MRI-based Attenuation Correction for PET/MRI

2.1. Background

As discussed in Chapter 1, the accuracy of attenuation correction of brain PET in PET/MRI studies is still questionable. Therefore, commercial simultaneous PET/MR scanners use several attenuation correction techniques rather than one solution method.

The first simultaneous PET/MR scanner, Biograph mMR (Siemens Healthcare, Erlangen, Germany), offers different MRI-based attenuation correction (MR-AC) techniques depending on the imaging site.

For whole-body scans, 2-point Dixon MR sequence was proposed to classify soft tissue, fat tissue, lungs and background (38). In their method, threshold and basic image processing were determined to identify and separate the voxel corresponding to the each tissue. Although the results showed that there is a similar behavior to CT based attenuation correction, it is generally difficult to obtain an optimal threshold value due to non-uniform changes and noise. This sequence is also not recommended for brain applications, due to an underestimation of PET uptake results (39).

For brain scan, MR-AC using ultrashort echo time (UTE) MRI sequence derives the bone segment based on the difference between two MR images obtained at different echo times (ultrashort and typical times) (40, 41). However, the initial versions of the UTE sequence (i.e., mMR software version VB18P) yielded frequent segmentation errors at the boundary between soft tissue, bone and air, as well as misclassification of the ventricle as air (39, 42, 43). Although a recent upgrade of the software from VB18P to VB20P offers more reliable attenuation maps than before,

significant segmentation errors in the regions around the inferior part of the brain (i.e., sinus and lower skull structures) still exist. The images are compared in Figure 2-2. Moreover, considerable quantification errors because of the inaccurate UTE MR-AC have been reported in several articles (39, 42, 43).

In this study, we propose an advanced UTE MR-AC method that is based on a multiphase level-set algorithm (44-46) to provide more accurate attenuation maps than those currently used in brain PET/MRI studies. The quantitative accuracy of this new method, providing a three–segment (air, bone, and soft tissue) attenuation map, was compared with CT-based and mMR-providing attenuation corrections.

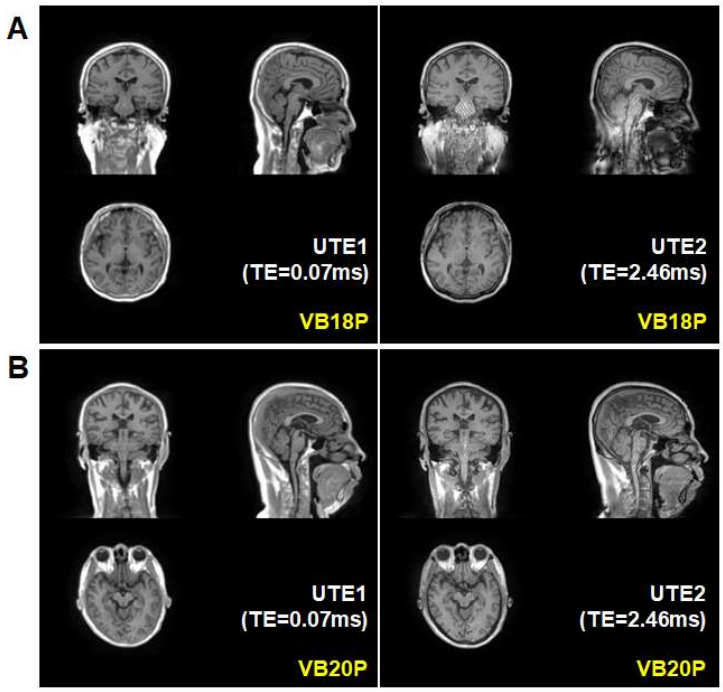

Figure 2-1. Comparision of UTE sequence images between (A) VB18P and (B) VB20P

2.2. Materials and Methods

2.2.1. Brain PET Dataset

2.2.1.1 Patient Population

We evaluated our new MR-AC method using two different brain PET data sets. One of them was the [^{18}F]fluorinated-N-3-fluoropropyl-2-β-carboxymethoxy-3-β-(4-iodophenyl)nortropane ([^{18}F]FP-CIT) PET/CT and PET/MRI data acquired for evaluating the accuracy of existing MR-AC methods in patients with Parkinson's disease. Total of 20 patients (11 men, 9 women, mean age: 59.6 ± 9.1 y, age range: 54–71 y) were enrolled in this study. The other was [^{18}F]fluorodeoxyglucose ([^{18}F]FDG) PET/CT and PET/MRI data of 10 prospectively enrolled healthy normal volunteers (6 men, 4 women, mean age: 57.7 ± 5.4 y, age range: 51–67 y) without any medical diseases or abnormalities uncovered in neuropsychological screening tests.

2.2.1.2 PET/CT and PET/MRI Acquisition

PET/CT data were acquired using a Siemens Biograph TruePoint40 scanner (Siemens Healthcare, Knoxville, TN) in [^{18}F]FP-CIT studies and a Siemens Biograph mCT40 scanner in [^{18}F]FDG studies. A Siemens Biograph mMR system was used for PET/MRI data acquisition in both studies. While the mMR software version of VB18P was used in the [^{18}F]FP-CIT studies, the software was upgraded to VB20P for the [^{18}F]FDG studies. The VB20P is the latest version, and provides improved UTE image quality by incorporating gradient delay correction, streak artifact suppression and a more advanced MR-AC method. In this new version skull segment is generated using template based approach and combined with the soft tissue map obtained by applying MRI segmentation.

In the [^{18}F]FP-CIT studies, a PET/MRI scan was performed 110 min after the injection of a tracer (192 MBq on average) and followed by a PET/CT scan. In the [^{18}F]FDG studies, the sequence of PET/MRI and PET/CT were randomly determined, and the first scan was performed 40 min after the injection of the tracer (259 MBq on average). PET scan duration for [^{18}F]FP-CIT and [^{18}F]FDG was 10 min.

2.2.1.3 PET/CT Data

PET/CT imaging was performed in a single PET bed position and the participants' heads were positioned in a head holder attached to the patient bed. The PET/CT scan followed the routine clinical protocol for brain studies including a topogram scan, an attenuation CT scan and a 10 min PET emission scan. For PET attenuation correction, the CT images were reconstructed in a 512 × 512 × 112 matrix with voxel sizes of 0.59 × 0.59 × 3 mm. The emission PET data were acquired in sinogram format.

2.2.1.4 PET/MR Data

In PET/MRI, the participants' heads were positioned in the mMR head coil. MR images were acquired simultaneously with PET using a dual-echo UTE sequence (TE = 0.07 and 2.46 ms, TR = 11.9 ms, flip angle = 10°). The UTE images were reconstructed into a 192 × 192 × 192 matrix with an isotropic voxel size of 1.33 mm. A T1-weighted 3D ultrafast gradient echo sequence was also acquired in a 208 × 256 × 256 matrix with voxel sizes of 1.0 × 0.98 × 0.98 mm

2.2.2. MR-Based Attenuation Map using Level-Set Algorithm

2.2.2.1. Level-set Segmentation Algorithm

In the past few decades, deformable active contour models have been widely used in image processing, especially for medical image segmentation. It is the curve deformed and moved under the influence of external and internal forces.

The level-set method, also known as the geometric deformable model, implicitly represents the contour by the zero level of a high-dimensional function called the level-set function $\phi(x, y, t)$. If this contour moves in the normal direction with a speed *F*, then the level set function satisfies the below level set equation,

$$\frac{\partial \phi}{\partial t} + F\left|\nabla \phi\right| = 0 \qquad (2.1)$$

where the function *F* is called the speed or energy functional that controls the motion of the contour. This approach has advantages over traditional segmentation methods such as thresholding and region growing, as it has the ability to represent contours with complex topology and to change their topology in a natural way.

In a variation of the level-set formulation, Chan et al. (44) proposed an active contour model using level-set formulation by incorporating region-based information. Assuming *I* is a two-dimensional (2D) image defined on domain Ω, the energy functional that we will minimize is defined as,

$$F^{CV}(\phi, c_1, c_2) = \int_{\Omega} \left|I(\mathbf{x}) - c_1\right|^2 H(\phi(\mathbf{x}))d\mathbf{x} + \int_{\Omega} \left|I(\mathbf{x}) - c_2\right|^2 (1 - H(\phi(\mathbf{x}))d\mathbf{x} + \nu \int_{\Omega} \left|\nabla H(\phi(\mathbf{x}))\right| d\mathbf{x},$$

$$H(z) = \begin{cases} 1, & \text{if } z \geq 0 \\ 0, & \text{if } z < 0 \end{cases},$$

$$\begin{cases} c_1(\phi) = \text{average}(I(\mathbf{x})) \text{ in } \{\phi \geq 0\} = \dfrac{\int_{\Omega} I(\mathbf{x}) H(\phi(\mathbf{x})) d\mathbf{x}}{\int_{\Omega} H(\phi(\mathbf{x})) d\mathbf{x}} \\ c_2(\phi) = \text{average}(I(\mathbf{x}))\text{n } \{\phi < 0\} = \dfrac{\int_{\Omega} I(\mathbf{x})(1 - H(\phi(\mathbf{x}))) d\mathbf{x}}{\int_{\Omega} (1 - H(\phi(\mathbf{x}))) d\mathbf{x}}. \end{cases} \quad (2.2)$$

where H is the Heaviside function and c_1, c_2 are the average image intensities in the contour, depending on I and ϕ. Image segmentation is achieved by solving to minimize the energy functional F_{CV}.

For the segmentation of more than two regions, Vese et al. (45) proposed a multiphase level-set approach. Theoretically, N level sets are used to segment up to 2^N regions. In particular, here we used a two-phase level-set method with the functions denoted as ϕ_1, ϕ_2 and the energy functional as the following,

$$\begin{aligned} F_4^{CV}(\Phi, \mathbf{C}) = & \int_{\Omega} |I(\mathbf{x}) - c_{11}|^2 H(\phi_1) H(\phi_2) d\mathbf{x} + \int_{\Omega} |I(\mathbf{x}) - c_{10}|^2 H(\phi_1)(1 - H(\phi_2)) d\mathbf{x} \\ & + \int_{\Omega} |I(\mathbf{x}) - c_{01}|^2 (1 - H(\phi_1)) H(\phi_2) d\mathbf{x} + \int_{\Omega} |I(\mathbf{x}) - c_{00}|^2 (1 - H(\phi_1))(1 - H(\phi_2)) d\mathbf{x}. \\ & + \nu \int_{\Omega} |\nabla H(\phi_1(\mathbf{x}))| d\mathbf{x} + \nu \int_{\Omega} |\nabla H(\phi_2(\mathbf{x}))| d\mathbf{x}, \end{aligned}$$

$$\begin{cases} c_1(\phi) = \text{average}(I(\mathbf{x})) \text{ in } \{\phi \geq 0\} = \dfrac{\int_{\Omega} I(\mathbf{x}) H(\phi(\mathbf{x})) d\mathbf{x}}{\int_{\Omega} H(\phi(\mathbf{x})) d\mathbf{x}} \\ c_2(\phi) = \text{average}(I(\mathbf{x}))\text{n } \{\phi < 0\} = \dfrac{\int_{\Omega} I(\mathbf{x})(1 - H(\phi(\mathbf{x}))) d\mathbf{x}}{\int_{\Omega} (1 - H(\phi(\mathbf{x}))) d\mathbf{x}}. \end{cases} \quad (2.3)$$

where $C=(c_{11},c_{10},c_{01},c_{00})$ is constant vector, and $\Phi=(\phi_1, \phi_2)$ is level set function vector. However, the Chan-Vese model is based on the assumption of intensity homogeneity. Therefore, local magnetic inhomogeneities and susceptibility effects can cause segmentation errors in MR images.

To address the issue of intensity inhomogeneity in MR image segmentation, Li et al. (46) proposed an improved level-set model with a local clustering criterion function. This method describes an image with intensity inhomogeneity, defined as follows:

$$I = bJ + n, \tag{2.4}$$

where I is the observed image, J is the true image, b is the bias field, and n is additive noise. The method is applied in a circular area with a radius ρ centered at each point y in the image domain Ω, defined by $O_y \triangleq (x:|x-y| \leq \rho)$ Then, each small region is given by:

$$b(\mathbf{x})J(\mathbf{x}) \approx b(\mathbf{y})c_i \quad \text{for} \quad x \in O_y \bigcap \Omega_i \ , \tag{2.5}$$

where the constant $b(\boldsymbol{y})c_i$ can be considered to be the approximation of the cluster center within the neighborhood O_y. To estimate $b(\boldsymbol{y})c_i$, the intensities $I(\boldsymbol{x})$ in the neighborhood O_y are classified into N classes. A local intensity criterion function using the K-means clustering method is defined as follows:

$$\varepsilon_y = \sum_{i=1}^{N} \int_{\Omega_i} K(\mathbf{y}-\mathbf{x}) \left| I(\mathbf{x}) - b(\mathbf{y}) c_i \right|^2 d\mathbf{x},$$

$$K(u) = \begin{cases} \dfrac{1}{a} e^{-|u|^2 / 2\sigma^2}, & \text{for } |u| \le \rho, \\ 0, & \text{otherwise} \end{cases} \qquad (2.6)$$

where $b(\mathbf{y})c_i$ are the cluster centers to be optimized, $K(\mathbf{y}-\mathbf{x})$ is a nonnegative weighting function, and a is normalization constant such that $\int K(u) = 1$. The intensity criterion function is integrated over the entire domain Ω and incorporated into a multi-phase level-set formulation given by:

$$F(\phi, \mathbf{c}, b) = \varepsilon(\phi, \mathbf{c}, b) + \nu \int |\nabla H(\phi)| d\mathbf{x} + \mu R_p(\phi),$$

$$\varepsilon(\phi, \mathbf{c}, b) = \int \sum_{i=1}^{N} \left(\int K(\mathbf{y}-\mathbf{x}) \left| I(\mathbf{x}) - b(\mathbf{y}) c_i \right|^2 d\mathbf{y} \right) M_i(\phi(\mathbf{x})) d\mathbf{x},$$

$$R_p(\phi) = \frac{1}{2} \int p(|\nabla \phi| - 1)^2 d\mathbf{x} \ . \qquad (2.7)$$

where $M_1(\phi(x)) = H(\phi(x))$ and $M_2(\phi(x)) = 1 - H(\phi(x))$ in the two-phase case. $R_p(\phi)$ is distance regularization term to make level set function smoothly. By minimizing this energy, we obtained the image segmentation result given by the level-set function and the estimation of the bias field *b*. In this work, we employed this energy model to segment images using the same parameters as in reference (46), μ=0.1, ν=0.001, and σ=4 .

2.2.2.2. Characteristic of UTE Images

The T2 relaxation time of protons in bone tissue is much faster than in other tissues. Thus, bone tissues with short T2 can be distinguished from soft tissue by taking the subtraction or division between the first ultrashort TE image (UTE1) and the second longer TE image (UTE2). However, these images, especially UTE2, are sensitive to off-resonance effects because of B_0 inhomogeneity and susceptibility, causing inhomogeneity artifacts that make accurate image segmentation difficult. Thus, we generated UTE MR-based attenuation map based on a level-set algorithm in which the intensity inhomogeneity correction was incorporated. These procedures were performed using in-house-developed code written in Matlab (R2014a; MathWorks, Natick, MA).

2.2.2.3. UTE Image Segmentation using Level-Set Algorithm

Two-phase level-set segmentation based on the multiphase model was applied to both the UTE1 and UTE2, in which two level-set functions were evolved simultaneously. Local intensity clustering properties as well as region-based information were taken into account to unify the segmentation and inhomogeneity correction within a single evolving framework. Figure 2-2 shows the results of the level-set segmentation. The final evolved contours (red: level-set function 1 = 0, blue: level-set function 2 = 0) are overlaid on the MR images. The regions delimitated by the contours were represented in the binary images by assigning one to the inside of the contour and zero to the outside (U_xL_y is the binary image from the y^{th} level-set function of the x^{th} UTE in Figure 2-2. The symbol 'C' labeled behind y indicates that the binary image is generated with inhomogeneity correction).

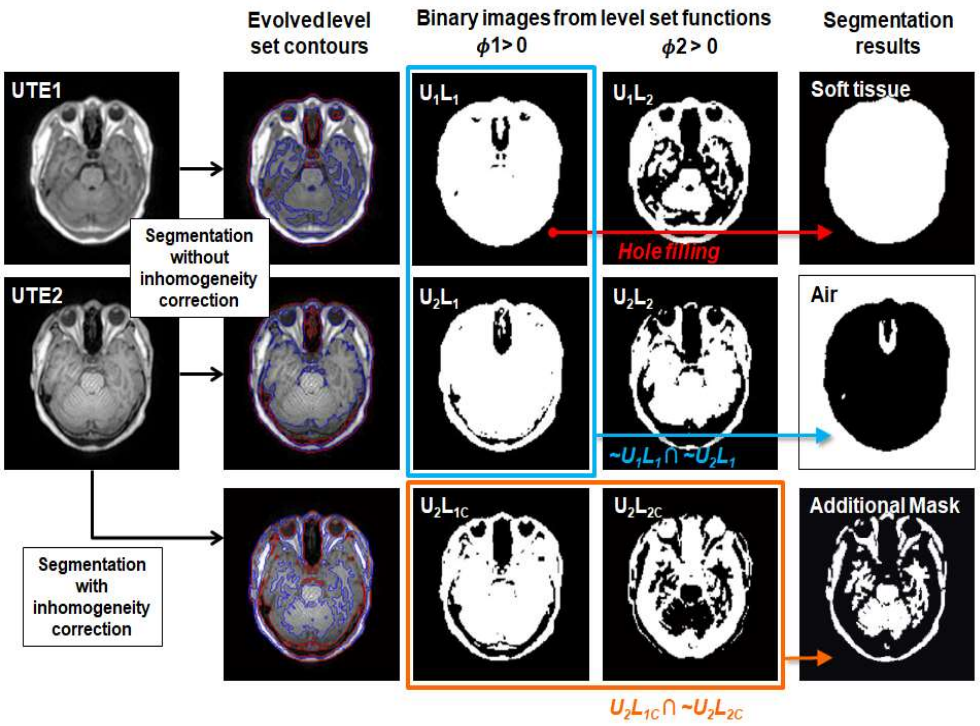

Figure 2-2. Generation of soft tissue and air maps and an additional mask using two-phase level segmentation and morphological and binary operations. The final evolved contours (red: level-set function 1 = 0, blue: level-set function 2 = 0) are overlaid on the MR images. U_xL_y is the binary image from the x^{th} level-set function of the y^{th} UTE. The soft tissue and air maps were generated by filling the holes in U_1L_1 and multiplying two binary images ($\sim U_1L_1$ and $\sim U_2L_1$). Additionally, a mask for trimming the bone map was generated from the binary images of the level-set functions obtained using the level-set segmentation with inhomogeneity correction ($U_2L_{1C} \cap \sim U_2L_{2C}$).

2.2.2.4. Generation of Attenuation Map

The soft tissue map was obtained by applying a hole-filling operation to the U_1L_1 that encloses almost all of the structures in the head. Air has a negligibly low signal in both UTE images. Thus, we obtained an air map by multiplying $\sim U_1L_1$ and $\sim U_2L_1$ in Figure 2-2. To generate the bone map, we started from the initial bone map generated by applying a threshold to the difference image (dUTE) between UTE1 and UTE2 represented in Figure 2-3. The threshold was empirically determined and 50% of the mean intensity of dUTE pixels >10. This initial bone map was then

masked by the morphologically eroded soft tissue map to correct for the misclassified voxels around the outer boundary of the skull with air. To further trim out the remaining misclassified soft tissue as bone in the dUTE image, we applied an additional mask generated by multiplying U_2L_{1C} and $\sim U_2L_{2C}$ (Figure 2-2 and 2-3). Finally, we added the bone segment to the initial attenuation map, and assigned the attenuation coefficients for soft tissue and bone (0.1 cm^{-1} and 0.151 cm^{-1}).

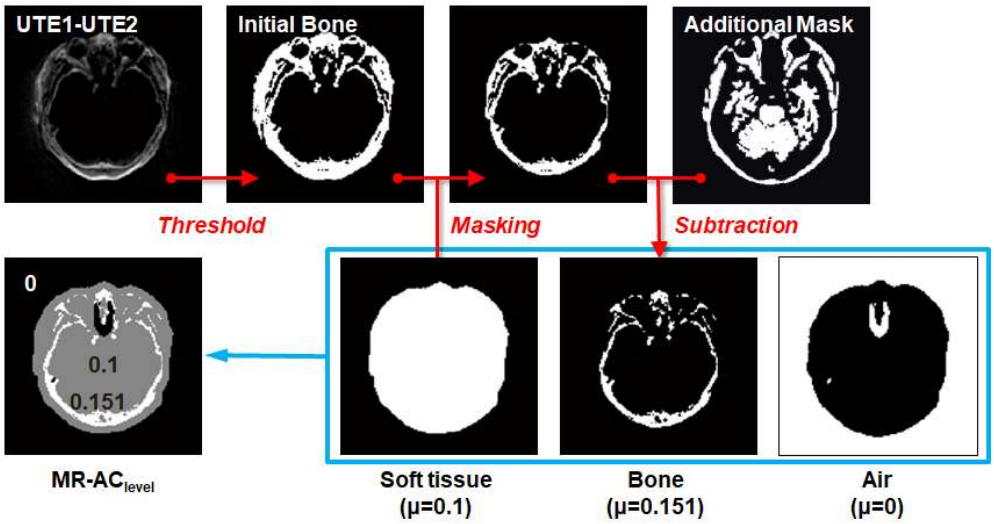

Figure 2-3. Generation of bone map and final level-set-based attenuation map (MR-AC_{level}). Initial bone map generated by applying a threshold to the difference image between UTE1 and UTE2 was further trimmed to yield the final bone map by masking it with soft tissue map and an additional mask. The MR-AC_{level} map was then generated by assigning the attenuation coefficients to the soft tissue, bone, and air maps and combining them.

2.2.3. Image Processing and Reconstruction

Reconstructed PET images were generated from emission data in the PET/CT studies using three different attenuation maps. The first one was the MR-based attenuation map that is offered by the Biograph mMR software (MR-AC_{mMR} map). The second one was the MR-based attenuation map generated using the proposed multiphase level-set method (MR-AC_{level} map). The last one was the CT-based

attenuation map conventionally used in PET/CT studies, which was converted from the CT images to 511 keV attenuation coefficients using a bilinear transformation (CT-AC map).

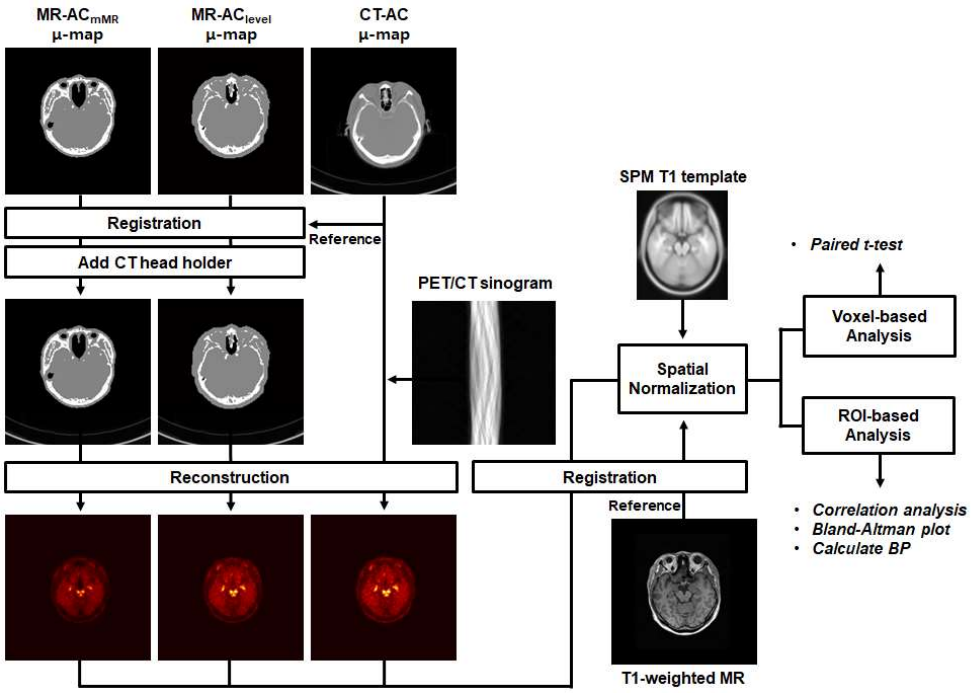

Figure 2-4. The overall procedure of image processing and PET reconstruction

For each participant, two MR-based attenuation maps were coregistered and resliced to the CT-AC map using the Statistical Parametric Mapping (SPM8; University of College London, UK) software through the co-registration of T1 3D MRI to CT. The PET/CT head holder was visible in the CT-AC map, whereas the UTE images were without the head holder. Therefore, the head holder shown in CT image was extracted using a region growing segmentation algorithm and added to the MR-based attenuation maps to allow a fair comparison. All PET images were reconstructed using OP-OSEM (subset = 14, iteration = 3) algorithm through e7tool

from Siemens Healthcare. Following reconstruction, all PET data were spatially normalized to the SPM standard MRI T1 template to eliminate intersubject anatomic variability. The overall image processing steps are summarized in Figure 2-4.

2.3. Results

The results of CT-AC, MR-AC_{mMR} and MR-AC_{level} applied to the same emission data acquired using PET/CT machines are compared in Figure 2-5 for [^{18}F]FP-CIT PET with VB18P mMR software and Figure 2-6 for [^{18}F]FDG PET and VB20P. The MR-AC_{mMR} map gave larger air cavities than CT regardless of the version of mMR software. The bone tissue in the MR-AC_{mMR} map was underestimated in VB18P (Figure 2-5B) and overestimated in VB20P (Figure 2-6B). On the contrary, MR-AC_{level} maps (Figures 2-5C and 2-6C) showed more similar properties with CT (Figures 2-5A and 2-6A) in the size and shape of the air cavities and bones. While the striatal and cerebellar activity in [^{18}F]FP-CIT PET and frontal activity in [18F]FDG PET were remarkably underestimated in MR-AC_{mMR} relative to CT-AC (Figures 2-5B and 2-6B), MR-AC_{level} did not show this discrepancy from CT-AC (Figures 2-5C and 2-6C).

The Dice similarity coefficients between MR-AC maps and CT-AC map were summarized in Table 2-1. The mean Dice coefficients for bone in MR-AClevel were 0.60 and 0.79 (VB18P and VB20P) for whole head and 0.71 and 0.83 for cranial region only, and all of them were higher than those in MR-AC_{mMR}. There was same trend for air regions.

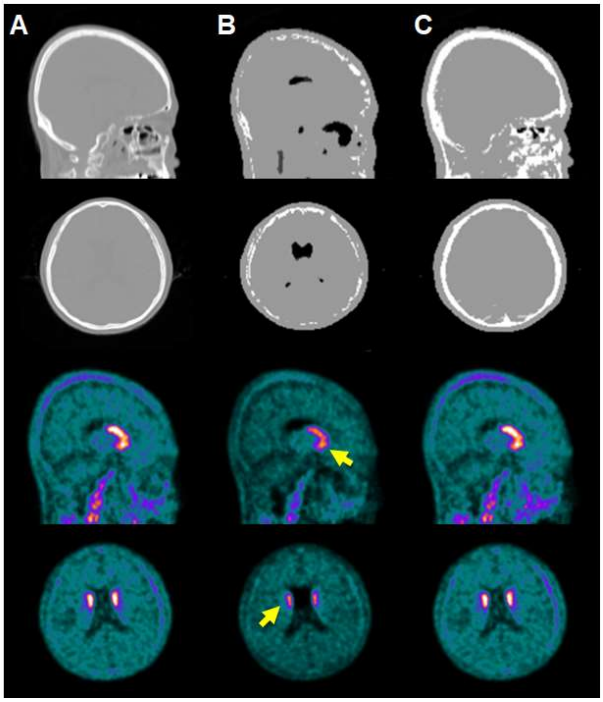

Figure 2-5. Attenuation maps and [^{18}F]FP-CIT PET images corrected using them. (A) CT, (B) MR-AC$_{mMR}$: MR-based attenuation map generated using mMR software version VB18P, (C) MR-$_{level}$: MR-based attenuation map generated using level-set method.

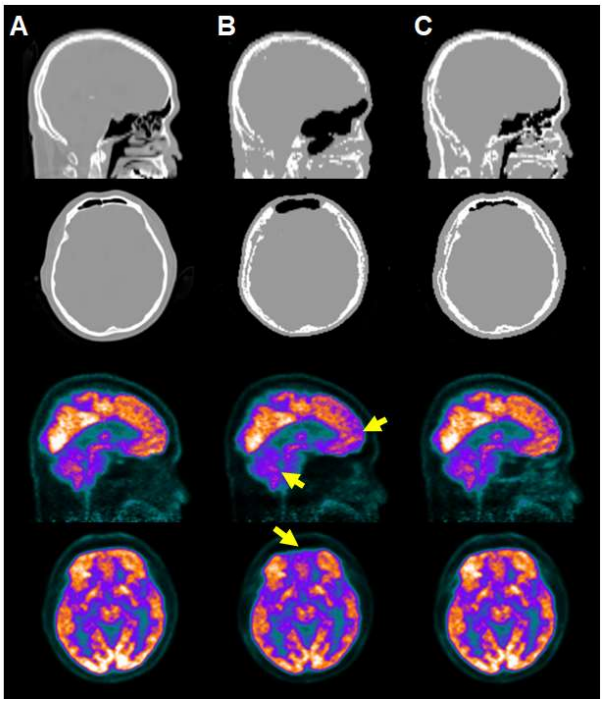

Figure 2-6. . Attenuation maps and [^{18}F]FDG PET images corrected using them. (A) CT, (B) MR-AC$_{mMR}$ using mMR software version VB20P, (C) MR-AC$_{level}$.

Table 2-1. Dice similarity coefficients for whole head and cranial bone (mean ± standard deviation)

	Whole head		Cranial region	
	D_{bone}	D_{air}	D_{bone}	D_{air}
[^{18}F] FP-CIT study (n=20)				
MR-AC$_{mMR\ (VP18P)}$	0.28 (±0.09)	0.45 (±0.10)	0.31 (±0.11)	0.42 (±0.10)
MR-AC$_{level}$	0.60 (±0.06)	0.54 (±0.09)	0.71 (±0.06)	0.59 (±0.08)
[^{18}F] FDG study (n=10)				
MR-AC$_{mMR\ (VP20P)}$	0.72 (±0.04)	0.60 (±0.06)	0.74 (±0.04)	0.59 (±0.09)
MR-AC$_{level}$	0.79 (±0.02)	0.61 (±0.07)	0.83 (±0.02)	0.62 (±0.10)

The superiority of MR-AC$_{level}$ to MR-AC$_{mMR}$ was confirmed in the ROI- and voxel-based quantitative comparisons. In [^{18}F]FP-CIT studies with MR-AC$_{mMR}$, the percent difference of SUV from CT-AC was greater than –20% in most ROIs (Figure 2-7A). The percent difference was most remarkable in cerebellum, leading to the overestimation of SUVr which was highest in putamen (Figure 2-7A). Conversely, the percent difference of [18F]FP-CIT PET with MR-AC$_{level}$ from CT-AC was smaller than 10% in both SUV and SUVr. The binding ratio (BR) values offered by the MR-AC methods were linearly correlated with those by CT-AC; nevertheless, the MR-AC$_{level}$ (putamen: $y = 1.04x \pm 0.016$, caudate: $y = 1.04x \pm 0.021$) yielded a smaller bias than MR-AC$_{mMR}$ (putamen: $y = 1.11x \pm 0.038$, caudate: $y = 1.14x \pm 0.073$) (Figures 2-8, 2-9 and 2-10).

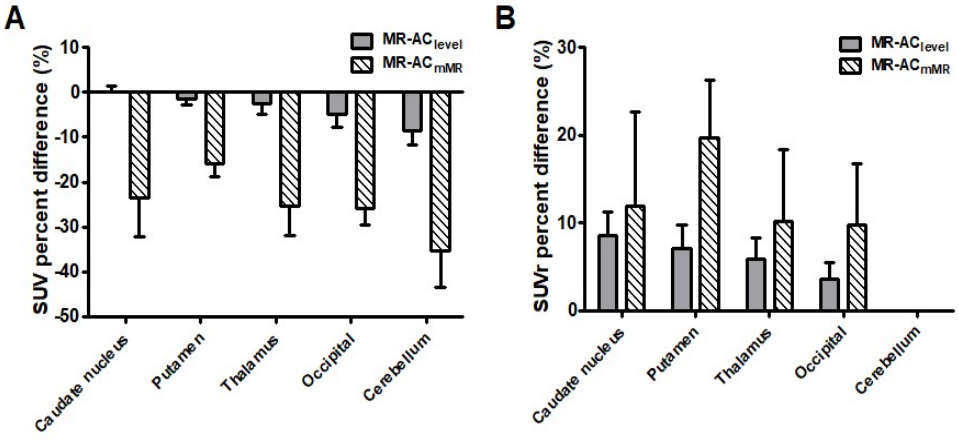

Figure 2-7. Percent difference of SUV (A) and SUVr (B) from CT-AC in [^{18}F]FP-CIT PET.

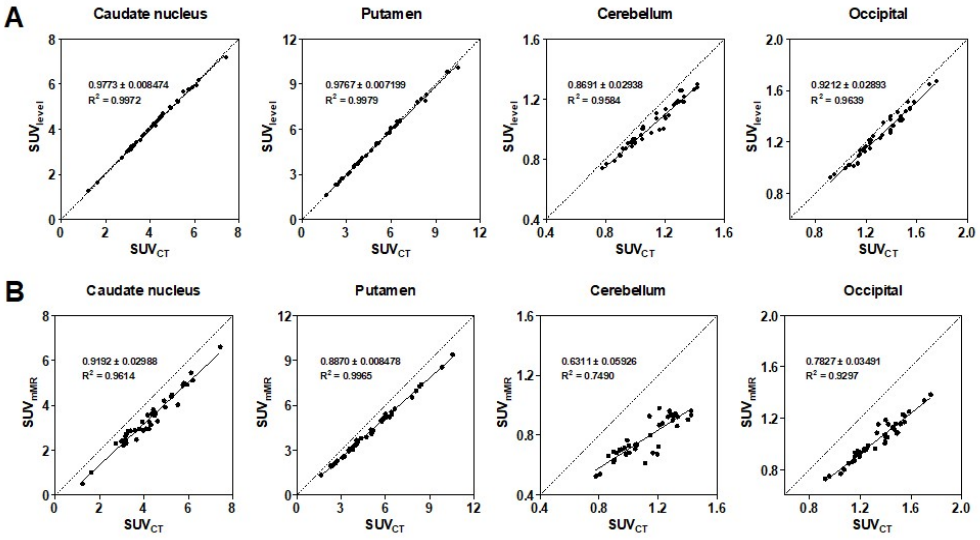

Figure 2-8. Correlation of SUV between CT-AC and (A) MR-AC$_{level}$, (B) MR-AC$_{mMR}$ in [^{18}F]FP-CIT study

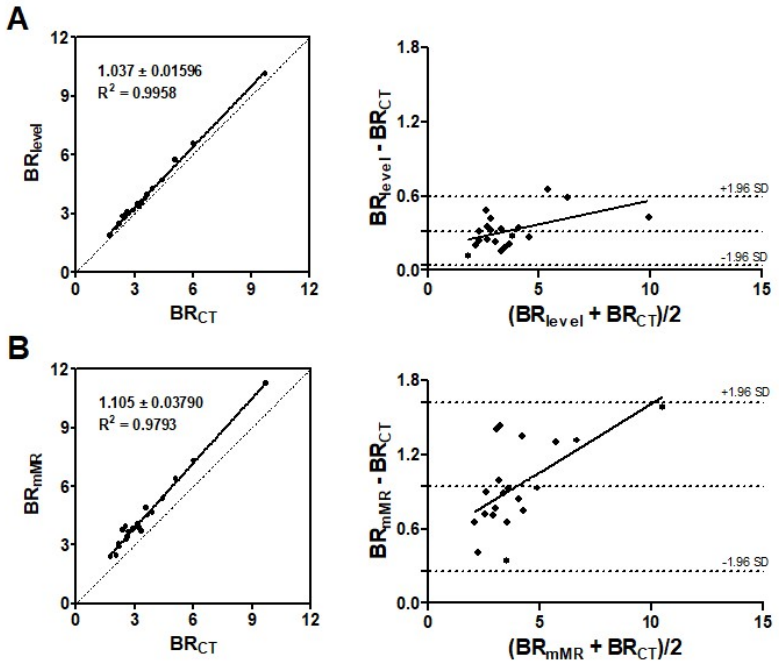

Figure 2-9. Correlation of binding ratio (BR) and Bland-Altman analysis in putamen between CT-AC and (A) MR-AC_{level}, (B) MR-AC_{mMR} in [^{18}F]FP-CIT study

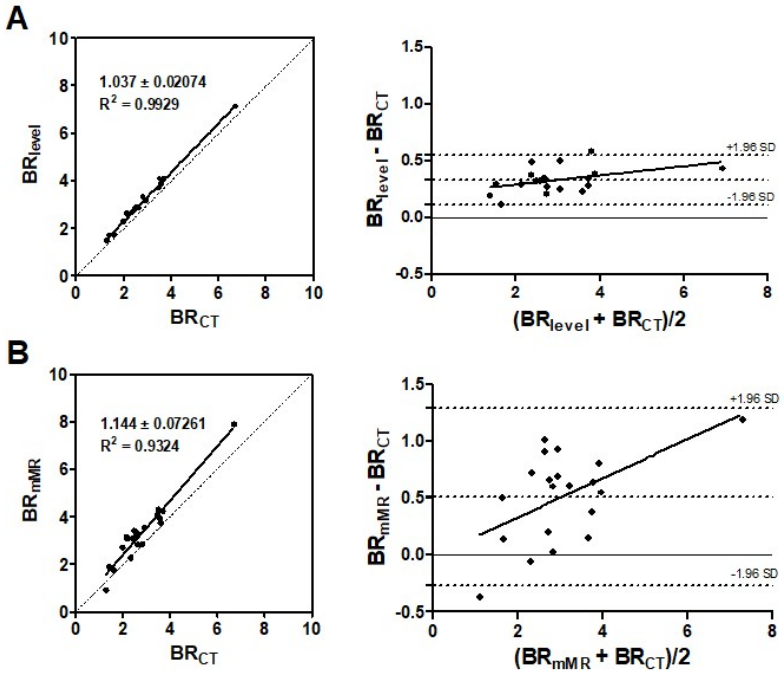

Figure 2-10. Correlation of binding ratio (BR) and Bland-Altman analysis in caudate nucleus between CT-AC and (A) MR-AC_{level}, (B) MR-AC_{mMR} in [^{18}F]FP-CIT study

The [^{18}F]FDG PET tests showed a similar trend to the [^{18}F]FP-CIT PET tests, while the percent differences in SUV and SUVr between MR-AC and CT-AC were roughly half of those in [^{18}F]FP-CIT PET (Figure 2-11, 2-12, and 2-13).

Figure 2-14 and 2-15 show that there was a remarkable difference in almost every brain regions voxel-wise comparison between MR-AC$_{mMR}$ and CT-AC. On the contrary the difference between MR-AC$_{level}$ and CT-AC was limited to the brain cortex. In both methods, outer boundary of brain cortex which is vulnerable to the brain size mismatch between CT and MRI and errors in skull segmentation showed largest differences.

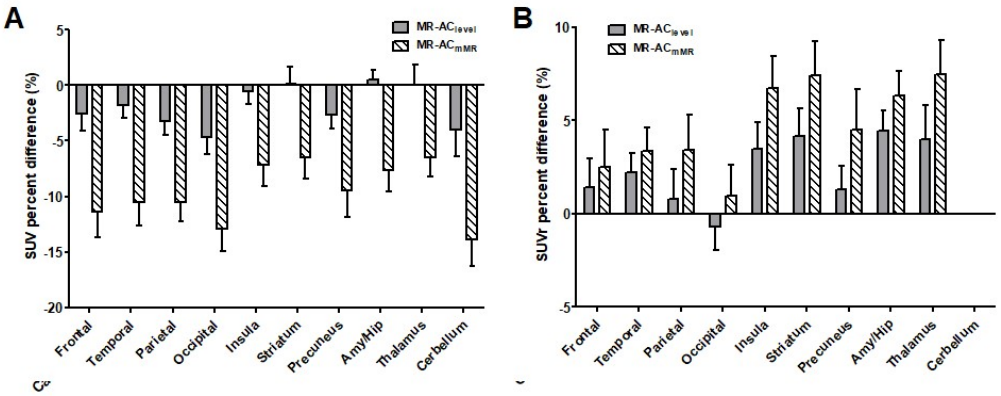

Figure 2-11. Percent difference of SUV (A) and SUVr (B) from CT-AC in [^{18}F]FDG PET.

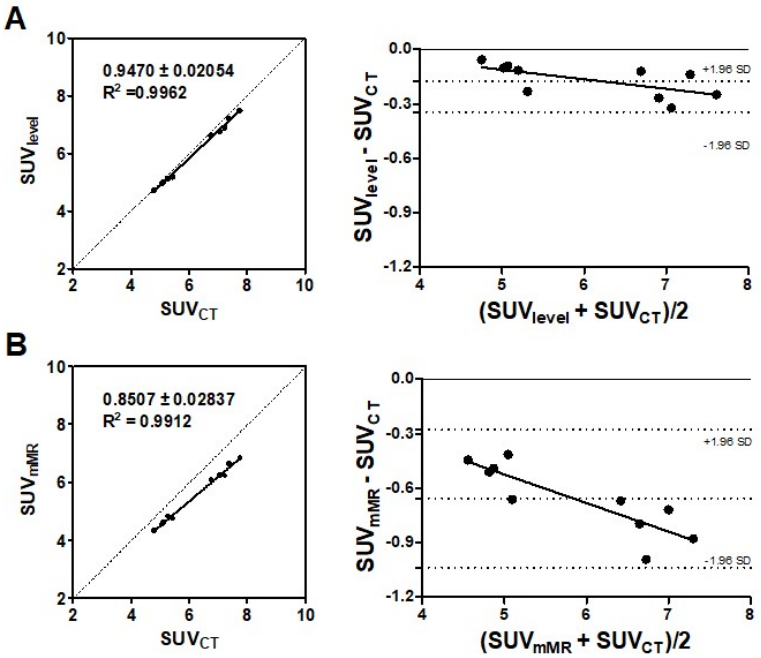

Figure 2-12. Correlation of binding ratio (BR) and Bland-Altman analysis in putamen between CT-AC and (A) MR-AC_{level}, (B) MR-AC_{mMR} in [^{18}F]FP-CIT study

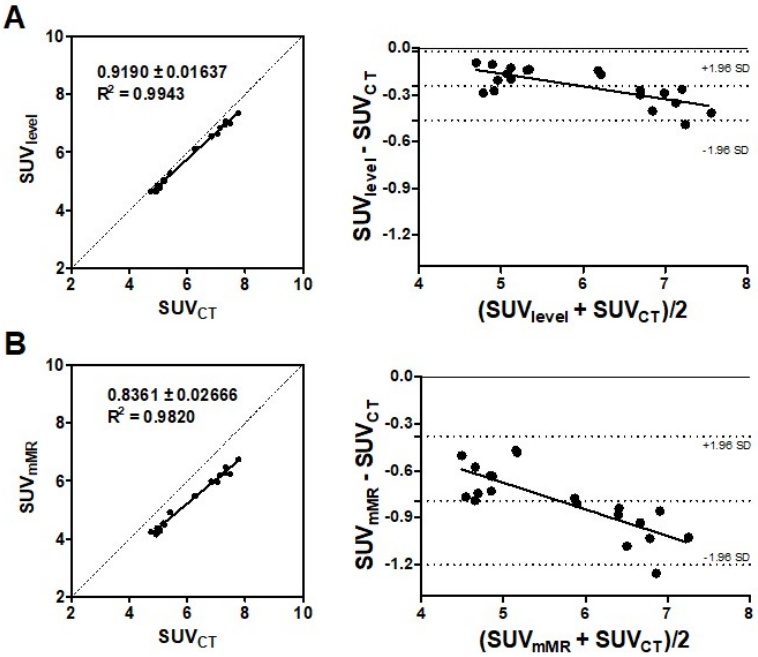

Figure 2-13. Correlation of binding ratio (BR) and Bland-Altman analysis in putamen between CT-AC and (A) MR-AC_{level}, (B) MR-AC_{mMR} in [^{18}F]FP-CIT study

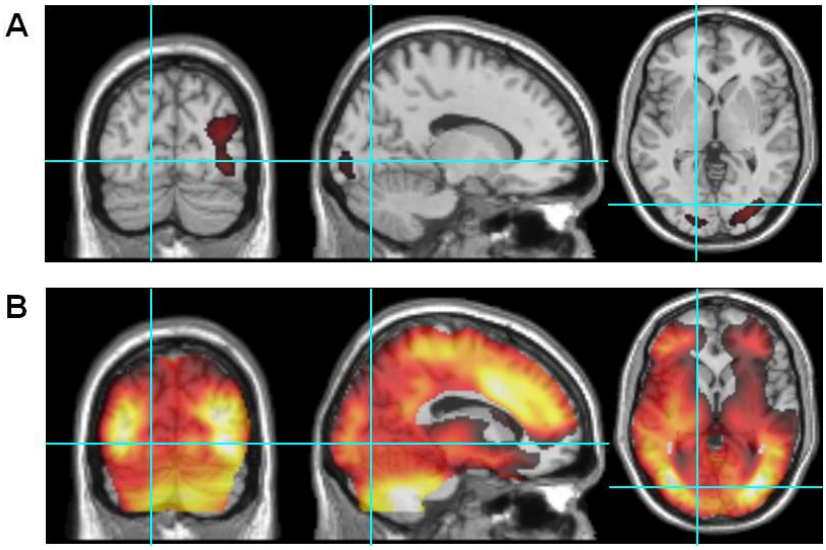

Figure 2-14. Paired t-test results of SUV in [^{18}F]FDG PET (A) CT-AC > MR-AC$_{level}$ (B) CT-AC > MR-AC$_{mMR}$ (P<0.05 (FWE), cluster size > 100 voxels).

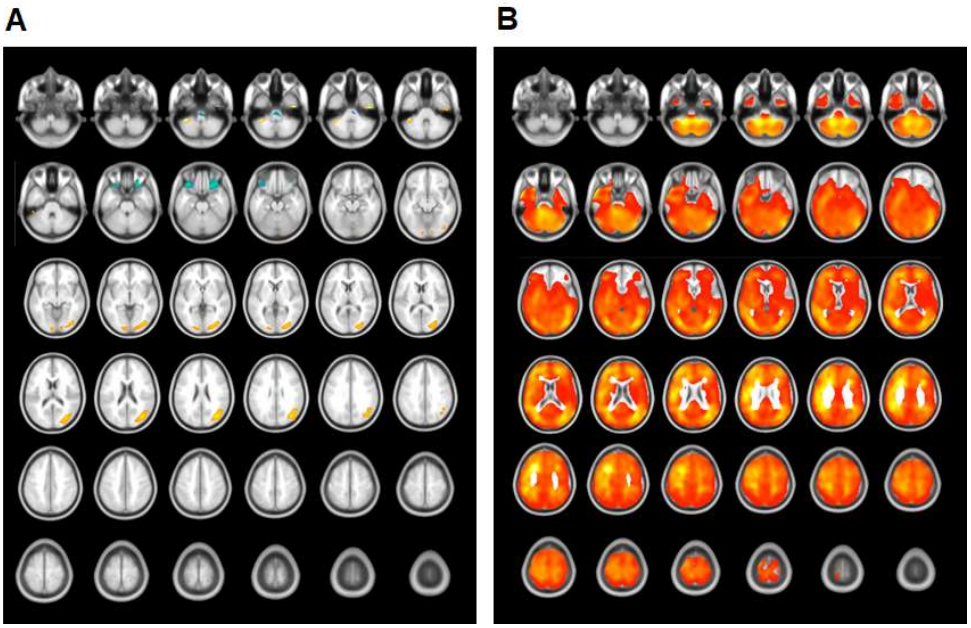

Figure 2-15. Paired t-test results of SUV in [^{18}F]FDG PET over whole brain data (A) CT-AC > MR-AC$_{level}$ (B) CT-AC > MR-AC$_{mMR}$ (P<0.05 (FWE), cluster size > 100 voxels).

2.4. Discussion

In this study, we developed a new UTE MR-AC map based on a unified multiphase level-set segmentation and inhomogeneity correction method, and demonstrated the superior performance of this method over the currently used MR-AC map in a mMR PET/MRI scanner. The remarkable improvements in the segmentation of air cavities and bone and the quantitative accuracy of PET measurement using the level-set method were shown in both the [^{18}F]FP-CIT PET data using VB18P mMR software and [^{18}F]FDG PET data using VB20P.

The major upgrade of mMR software from VB18P to VB20P seems to be effective in the elimination of misclassification of cerebrospinal fluid in ventricles as air and the correction of bone underestimation shown in previous reports. The percent error of MR-AC$_{mMR}$ in SUV and SUVr quantification relative to CT-AC was reduced approximately by half, although we could not confirm this error reduction using the exact same dataset. However, the current VB20P version still yields air cavity and bone segmentation errors as shown in Figure 2-6B. However, the MR-AC$_{level}$ offered improved segmentation results, leading to the reduction of PET quantification error by a factor of approximately three as shown in Figure 2-7.(SUV error < 10% in MR-AC$_{level}$ and < 30% in MR-AC$_{mMR}$ with VB18P, and < 5% in MR-AC$_{level}$ and < 15% in MR-AC$_{mMR}$ with VB20P). The evaluation of attenuation maps using Dice coefficient confirmed the improvements in the MR-AC maps achieved by the level-set method in Table 2-1. For VB20P UTE data sets, MR-ACl$_{evel}$ yielded the Dice coefficient for bone of 0.83 in cranial region while MR-AC$_{mMR}$ offered 0.74 in this study and 0.65 in other previous study.

The results suggest that UTE MR-AC$_{level}$ provides more accurate PET

quantification than Dixon-based AC methods that yielded around 10-20% errors in and 5%-15% in depending on brain regions (larger error in cortical regions). Recent advanced template-based approach and new approaches with R2* to HU conversion and zero-echo-time show similar results to our approach and/or great potential for further improvement of MR-AC. The combination of our approach with those methods would be the interesting next step that we can take to improve the MR-AC in brain and potentially in whole-body PET/MRI studies.

The advanced results using the level-set method can be attributed to the combined effects of various factors in this study. These factors include the inhomogeneity correction of UTE images incorporated into the level-set segmentation, which led to the more reliable segmentation results. The assorted boundary information provided by the multiphase level-set segmentations applied to both the UTE images were useful for determining the complex boundaries among different segments and trimming the segmentation results through morphological operations on the binary images.

Although MR-AC_{level} yielded almost equivalent SUV quantification results to CT-AC in most brain regions, the errors in cerebellum and occipital cortex were larger than in other regions (Figures. 2-7A and 2-11A). The errors in these most common reference regions in brain PET studies resulted in positive biases in BR and SUVr estimations (Figs. 2-7B and 2-11B, Figure 2-9 and 2-10). It is most likely that the errors in these posterior and inferior brain regions are related to the misclassification of fat tissues in the neck as bone. This misclassification, also observed in Figures 2-5C and 2-6C, is likely caused by the image intensity brightening at the periphery of UTE images mainly because of the inhomogeneous B1 field associated with multichannel phased array coils.

Chapter 3. MR-based synthetic CT generation for MR-IGRT

3.1. Background

The MRI is increasingly being used in radiotherapy because it provide superior soft tissue contrast to delineate tumors and soft tissues. It allows a more precise identification of target volume compare to CT and consequently reduce the margin expansion from clinical target volume to PTV during the treatment planning. This reduction of margin not only reduce the OAR dose, but also shows optimal dose coverage for the targe, which is particulary helpful for high dose an hypofractionation treastments such as SBRT and SABR (47).

Despite of several advantages of MRI, one major issue in MR-IGRT is the assignment of electron densities to MRI scans for dose calculation. Because the MR signals are related to the proton density and relaxation properties of tissue, not to electron density. As a result, additional CT imaging is essential to know the radiation dose distribution. The common strategy consists in applying rigid or deformable registration between MRI and CT simulation images and assigning electron density map obtained from the dCT that is shown in Figure 3-1.

However, there is risk of registration inaccuracy as a result the discrepancies in patient position, anatomical changes between scans. In order to overcome these difficulties, many attempts have been made to synthesize CT from MR images in various ways (24, 27-29, 48). Recently, deep learning-based model have been used to generate sCT after training of MR-dCT paired sets (32-36, 49, 50). However, these studies showed used dataset from diagnostic MR imaging rather than MR-IGRT system.

For this purpose, we aimed to develop a synthetic CT generation algorithm wih the deep learning method using MR-dCT paired set from MR-IGRT system. We investigated the accuracy of the proposed method and performed a dosimetric evaluation of sCT images compared to conventional dCT method.

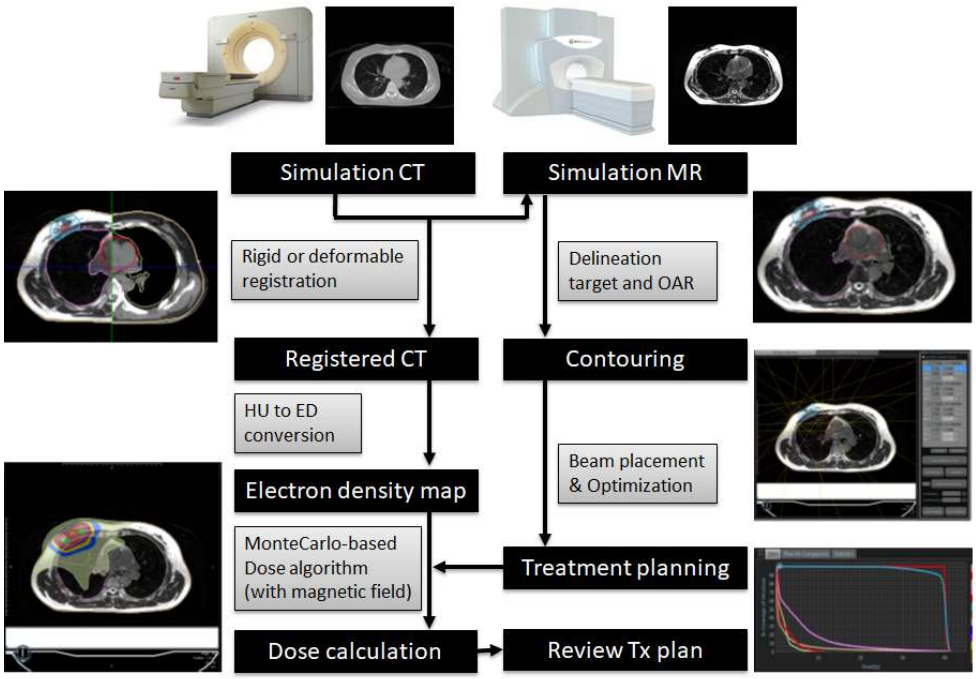

Figure 3-1. Schematic procedure of MR-IGRT treatment

3.2. Materials and Methods

3.2.1. MR-dCT Paired DataSet

3.2.1.1 Patient Selection

Total 90 patients data who underwent MR-IGRT were retrospectively considered. The study was approved by the institutional review board. The patients data can be divided into three categories, 30 with abdomen, 30 with thorax, and 30 with pelvis. In this study, a synthetic CT model was separately applied to datasets in each region. Table 3-1 summarizes patient characteristics.

Table 3-1. Summary of patient characteristics of MR-dCT paired dataset

Characteristics	Parameter	Value or Number of patient
For Abdomianl region (n=30)		
Age	Mean ± Std	66 ± 10
Sex	Male	19
	Female	11
Diagnosis	Pancreatic cancer	14
	Klatskin tumor	4
	Liver lymph node metastasis	4
	Hepatocellular carcinoma	3
	Gallbladder cancer	2
	Other	3
Treatment Technique	IMRT	17
	SBRT	13
Prescription dose	50 Gy / 5 fx	5
	45 Gy / 5 fx	5
	40 Gy / 5 fx	2
	37.5 Gy / 5 fx	1
	60 Gy / 30 fx	2
	56 Gy / 28 fx	4
	54 Gy / 27 fx	2
	50 Gy / 25 fx	5
	30 Gy / 5 fx	1
	27.5 Gy / 5 fx	1
	20 Gy / 5 fx	1
	40 Gy / 8 fx	1

For Thoracic region (n=30)		
Age	Mean ± Std	59 ± 5
Sex	M	0
	F	30
Diagnosis	Right breast cancer	18
	Left breast cancer	12
Treatment Technique	APBI using IMRT	30
Prescription dose	38.5 Gy / 10 fx	30

For Pelvic region (n=30)		
Age	Mean ± Std	74 ± 6
Sex	M	30
	F	0
Diagnosis	Prostate cancer	30
Treatment Technique	IMRT	9
	IMRT with SIB	13
	SBRT	8
Prescription dose	70 Gy / 28 fx	20
	62.5 Gy / 25 fx	2
	36.25 Gy / 5 fx	8

IMRT = Intensity Modulated Radiation Therapy, SBRT = Stereotactic Body Radiation Therapy, APBI = Accelerated partial breast irradiation, SIB = Simultaneous-integrated boost

3.2.1.2 CT and MR Image Acquisition

For the treatment planning, all patient MRI simulation scan was obtained 15 min after CT simulation scan, consecutively. The CT images were acquire using a Brilliance Big Bore CT scanner (Philips, Cleveland, OH). The MRIdian system (ViewRay, Oakwood, OH) was used for 0.35T MRI data acquisition. The MR images were acquired using a true fast imaging with steady-state precession (TrueFISP; TRUFI) sequence. The MRI scans were obtained with the same patient setup and the same immobilization device as the CT simulation. CT images were aligned to the corresponding MR images through deformable registration provided ViewRay TPS. After registration process, these registered dCT images were resampled to the same size of MR images. The accuracy of image registration was visually compared by the radiation oncologist and it was excluded from the dataset when the mismatch

occurred in the outer and inner contour of patient body.

3.2.1.3 Image Pre-processing

The workflow of image pre-processing before network training summarized in Figure 3-2. First, the dCT images were processed to remove external part of the dCT images, such as body frame and coil based on the body region of the MR images. Second, blurred image slices at the edges along the axial dimension based on MR image were excluded from the dataset. This work was applied to both MR and dCT dataset. Third, the center point artifact, which is often caused by MR calibration problem, was removed. A series of image pre-processing procedures were performed using an in-house Matlab (R2018a; MathWorks, Natick, MA) program. In addition, the 0.35T TRUFI sequence MR image intensities may vary between scans and can

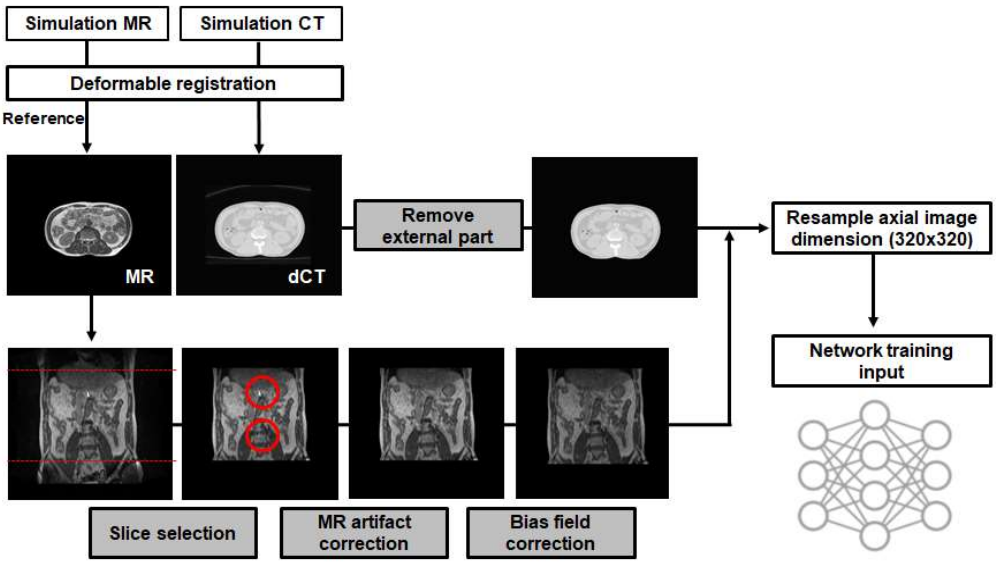

Figure 3-2.The workflow of image pre-processing.

also be affected by B_0 and B_1 field nonuniformities. Therefore, N4 bias field correction (51), available at open source 3D Slicer 4.6.2, was applied on the MR images to remove inhomogeneity.

The axial diemension of entire MR and dCT dataset was resampled to 320 x 320 matrix to fit into a CNN architecture. For learning network input, the MR images were normalized using a 95% percentile value of each image intensity in each patient, and CT images using the maximum value in each patient, respectvely.

Figure 3-3 shows a pair of MR and dCT images of pelvic, thoracic, abdominal region which all image processing has beem completed.

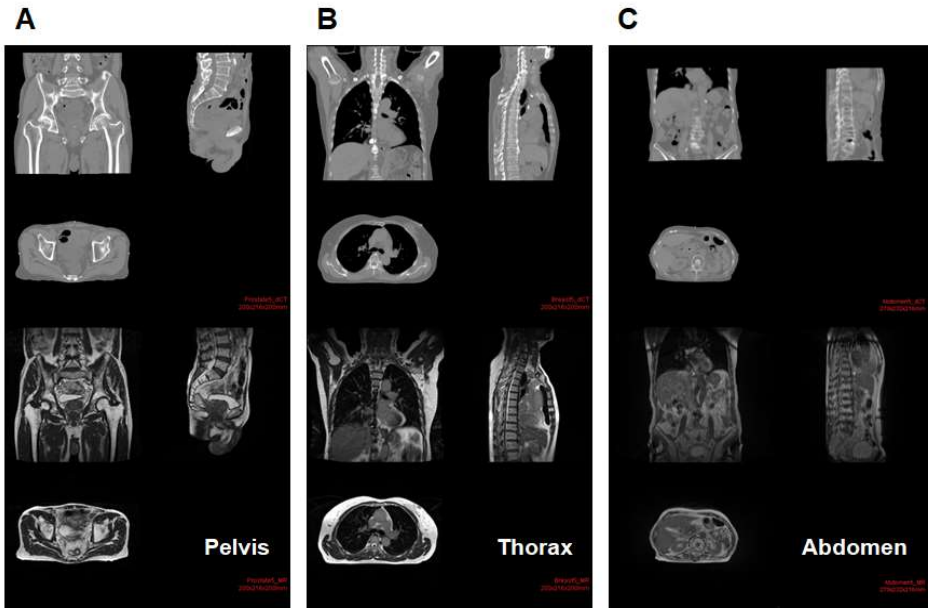

Figure 3-3. All image processed MR and dCT paired dataset of (A) Pelvis, (B) Thorax, (c) Abdomen

3.2.2. Synthetic CT Generation using 2D CNN

3.2.2.1 Network Architecture

We utilized 2D CNN to generate a synthetic CT image from paired MR-dCT dataset. The 2D CNN network, called U-net by the shape of learning structure, is well known successful network for medical image segmentation (52). In the U-net architecture, it has a symmetric structure consisting of contracting path and expanding path to have the same size as original input image. In addition, there is skip connections between contracting and expanding path to provide local information to the global information.

In this study, the 2D CNN U-net architecture introduced by Han (32) was adopted and modified. The leaky rectified linear unit (ReLU) was used as activation function instead of ReLU. A schematic overall architecture of 2D CNN U-net is depicted in Figure 3-4.

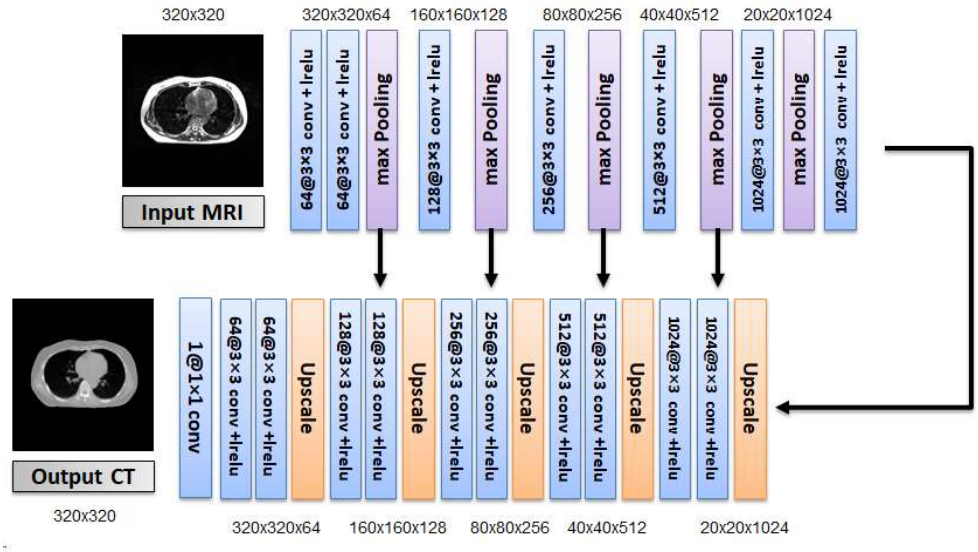

Figure 3-4. Overall architecture of 2D CNN U-net for generating synthetic CT

3.2.2.2 Network Training and Implementation

The network trained using 2D MR-dCT paired images along axial dimension. For each patient region, 24 MR-dCT paired dataset (80% of total paired dataset) were randomly selected as the training data and the other 6 paired dataset used as the validation data. Data augmentation was performed by flipping all images along the horizontal, vertical, and both direction to increas the number of training samples and improve generalization of the network. Therefore, we used 4 times the number of pre-processed dataset were used in training process. A total of 15246, 16860, and 9516 image slices were used for pelvic, thoracic, and abdominal region, respectively.

The learning network was implemented using Tensorflow framework (Tensorflow-gpu v1.14.0 and Python v3.6) on single NVIDIA Geforce GTX 1080Ti GPU card with 11 GB memory. The network trained 200 epochs with adaptive stochastic gradient descent optimizer with a learning rate of 0.0001. Weight and biases in the vonvolutional layers and decovolutional layer were trained by miniminzing a loss function. The loss function using as the mean absolute error (MAE) between the sCT and dCT is defined as,

$$\mathrm{L}_1 \text{ loss function} = \frac{1}{N}\sum_{i=1}^{N}\left|sCT_i - dCT_i\right| \qquad (3.1)$$

where i is a voxel within the body and N is the total number of voxels.

The sCT generation was performed by applying MR images of validation dataset to the trained network model. The HU value of sCT was restored considering the normailized value applied to each patient. Finally, sCT images were converted

DICOM format allowing use in the ViewRay TPS.

3.2.3. Data Analysis

3.2.3.1 Geometric Analysis

For each patient, the accuracy of the sCT was evaluated by calculating MAE, root mean square error (RMSE), and peak signal-to-noise ratio(PSNR) compared with dCT as follows:

$$MAE = \frac{1}{N}\sum_{i=1}^{N}\left|sCT_i - dCT_i\right| \tag{3.2}$$

$$RMSE = \sqrt{\frac{1}{N}\sum_{i=1}^{N}(sCT_i - dCT)^2} \tag{3.3}$$

$$PSNR = 10 \cdot \log_{10}\left(\frac{MAX^2}{MSE}\right) \tag{3.4}$$

where i is a voxel within the body, N is the total number of voxels, and MAX is the maximum pixel value of voxel.

We also calculated the structural similarity (SSIM), which evaluates the visual impact of the three characteristics such as luminance, contrast and structure. The simplified equation of SSIM is defined as,

$$SSIM = \frac{(2\mu_x\mu_y + c_1)(2\sigma_{xy} + c_2)}{(\mu_x{}^2 + \mu_y{}^2 + c_1)(\sigma_x{}^2 + \sigma_y{}^2 + c_2)} \tag{3.5}$$

where μ_x, μ_x,σ_x, σ_y and σ_{xy} are the local means, standard deviations, and cross-covariance for images of sCT and dCT.

3.2.3.2 Dosimetric Analysis

For dosimetric evaluation, the ViewRay TPS for tri-^{60}Co system was employed for treatment planning. With the sCT images, dose distribution calculated under the identical conditions as the dCT treatment plan. The dose distributions were calculated using the MonteCarlo algorithm with calculation grid size of 3mm and magnetic field correction included.

The prescription dose to PTV was not the same for all patient. In order to evaluate the dose distribution under the same condition, the scaling process for dose was calculated as follows : Pelvis 70 Gy, Thorax 38.5 Gy, Abdomen 50 Gy.

The comparison between sCT and dCT dose distribution was performed by calculating minimum (D_{min}), maximum (D_{max}) and mean (D_{mean}) absorbed doses for different critical organs and target volumes. In addition, The conformity index (CI) and the homogeneity index (HI) for each PTV were calculated as follows:

$$\text{Conformity index } (\text{CI}) = \frac{V_{100\%} \textit{ of the target volume}}{\textit{Volume of the target volume}} \qquad (3.6)$$

$$\text{Homogeneity index}(\text{HI}) = \frac{D_{2\%} - D_{98\%}}{\textit{mean dose}} \qquad (3.7)$$

To examine the difference between sCT and dCT calculated doses, we performed gamma index evaluation (53). Gamma index is a metric used for comparing two plans of dose distribution. It allows to express the difference between

the plans in a given point in space with a number, which is very important for performing patient quality assurance. The gamma index γ is defiend as,

$$\Gamma(r_m, r_c) = \sqrt{\frac{r^2(r_m, r_c)}{\Delta d_M^2} + \frac{\delta^2(r_m, r_c)}{\Delta D_M^2}} \tag{3.8}$$

$r(r_m, r_c) = |r_c - r_m|$: Distance between analyzed points

$\delta(r_m, r_c) = D_c(r_c) - D_m(r_m)$: Dose difference

The pass-fail criteria :

$\gamma(r_m) \le 1$, calculation passes, *(3.9)*

$\gamma(r_m) > 1$, calculation fails.

where r_m, r_c are the single measurement point and the spatical location of calculated distribution relative to the measurement point. The dose-difference criterion is Δd_M , and the distance-to-agreement(DTA) criterion is ΔD_M . The DTA is the distance between a measured data point and the nearest point in the calculated dose distribution that exhibits the same dose.

In this study, gamma criterion of 1 mm/1%, 2 mm/2% and 3 mm/ 3% were used and points with doses equal to or less than 10%, 50%, and 90% of the maximum dose in the dose distribution were not evaluated.

3.3. Results

3.3.1 Image Comparison

Pelvic region

The results of axial, sagittal, and coronal views of input MRI, dCT, and output sCT for pelvic region are shown in Figures 3-5, 3-7 and 3-8. The Figure 3-6A shows the HU comparison between dCT and sCT. The dCT and sCT profile transecting femur bone and prosate are shown at Figure3-6B. The HU values of dCT and sCT are represented in the solid and dash lines, respectively.

According to visual inspection, the sCT produced by 2D CNN matched closely to both soft tissue and bone structure compared to dCT. The absolute HU difference between CT and sCT is usually small, except for the discrepancy between the edge of the bone and the body surface. It can be seen that the air pocket and soft tissue close to the superior direction are generated from the structure of the MR image. Unlike the axial diemension, discontinuities in soft tisssue and bone were observed in coronal and sagittal dimension.

Thoracic region

The results of axial, sagittal, and coronal views of input MRI, dCT, and output sCT for thorax region are shown in Figures 3-9, 3-11 and 3-12. The Figure 3-10A shows the HU comparison between dCT and sCT. The dCT and sCT profile transecting both lungs, ribs, and mediastinum are shown at Figure 3-10B. The HU values of dCT and sCT are represented in the solid and dash lines, respectively.

The 2D CNN model achieved adequate HU prediction of sCT for soft tissue and spine. However, there were difficulties in the generating ribs, which can be also

found in the profile in Figure 3-10B. There was a slight overestimation of the sCT HU values as can been seen in the overall blueness in the HU differnece map in Figure 3-6A. As shown in Figure 3-11, it can be found that the difference HU values with discontinuity in the sagittal dimension.

Abdominal region

The results of axial, sagittal, and coronal views of input MRI, dCT, and output sCT for abdomen region are shown in Figures 3-13, 3-15 and 3-16. The Figure 3-14A shows the HU comparison between dCT and sCT. The dCT and sCT profile transecting liver, and stomach are shown at Figure 3-14B. The HU values of dCT and sCT are represented in the solid and dash lines, respectively.

Compared with the results of the previous two regions, the sCT of soft tissue and bone structure generated more blurred. Also, the discontinuity is easily obseved due to the change in the HU values in coronal dimension as shown in Figure 3-16. As shown in Figure 3-14A and 3-14B, it was observed that the sCT HU value of the overall area was overestimated in the HU difference map.

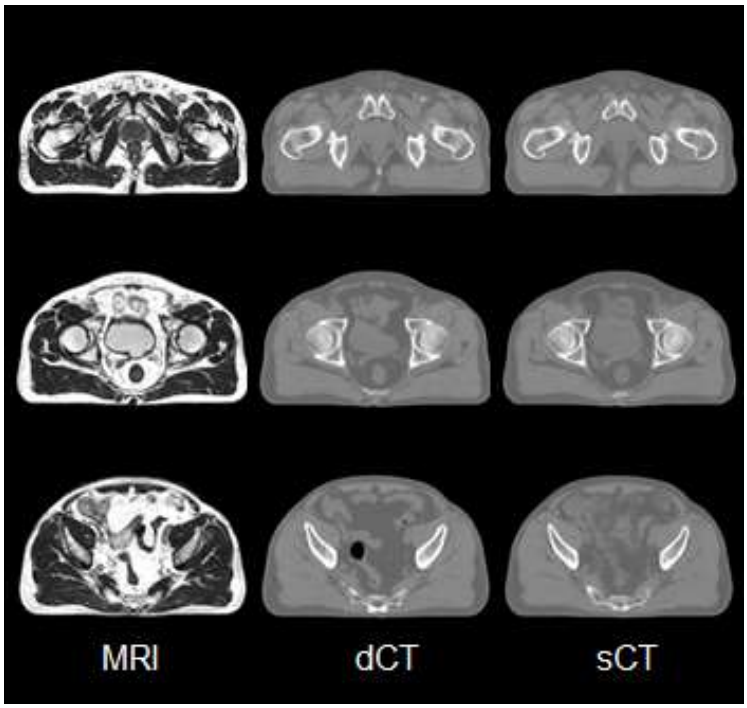

Figure 3-5. The representative axial slice views of MRI, dCT and sCT for pelvis

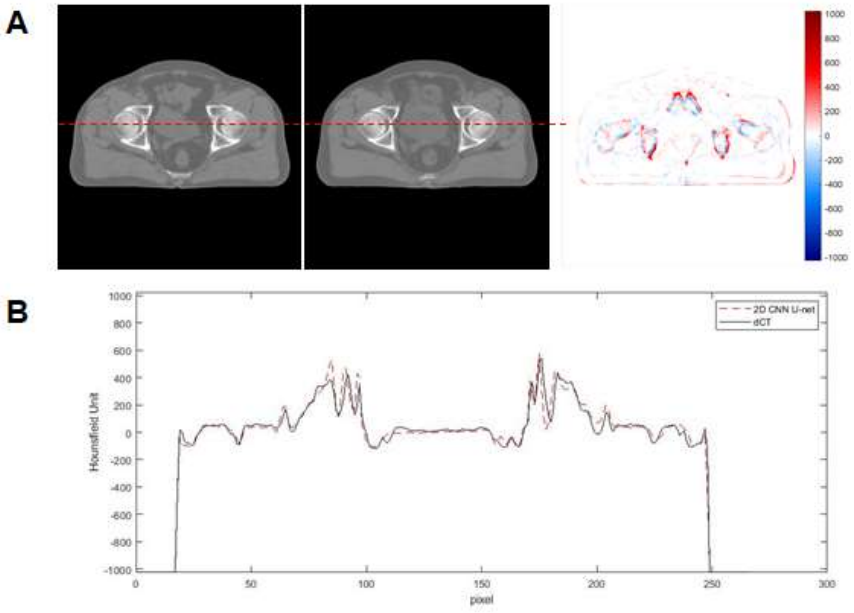

Figure 3-6. (A) The difference map between 2D CNN model sCT image and the dCT image for pelvis, (B) The voxel-based HU profile of sCT(dash line) and dCT (solid line)

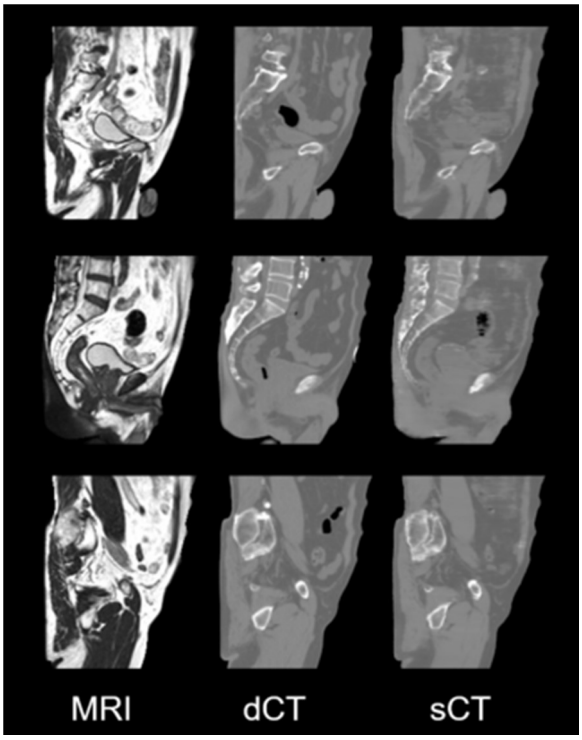

Figure 3-7. The representative sagittal slice views of MRI, dCT and sCT for pelvis

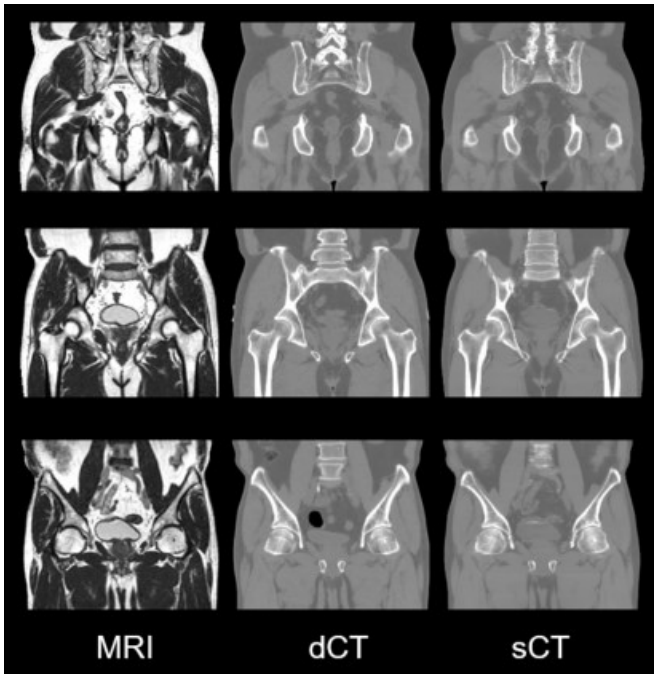

Figure 3-8. The representative coronal slice views of MRI, dCT and sCT for pelvis

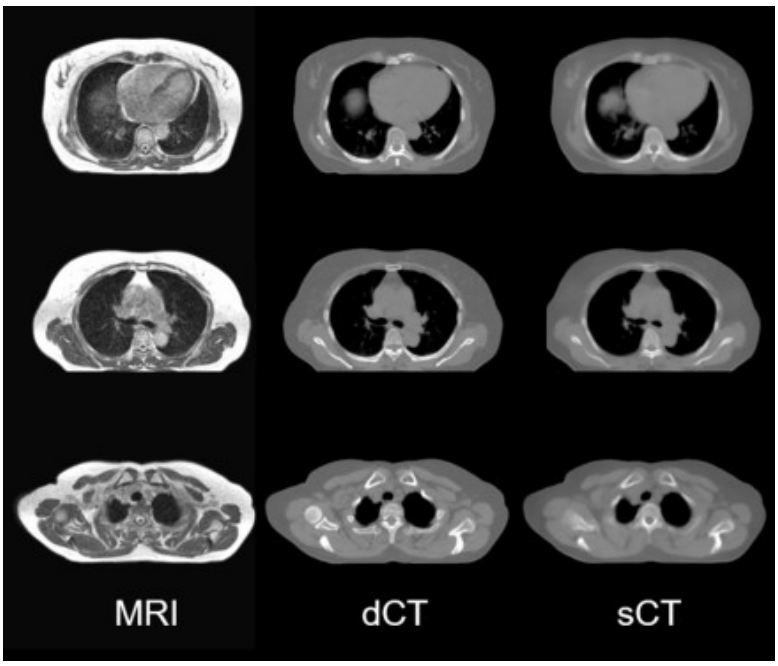

Figure 3-9. The representative axial slice views of MRI, dCT and sCT for thorax

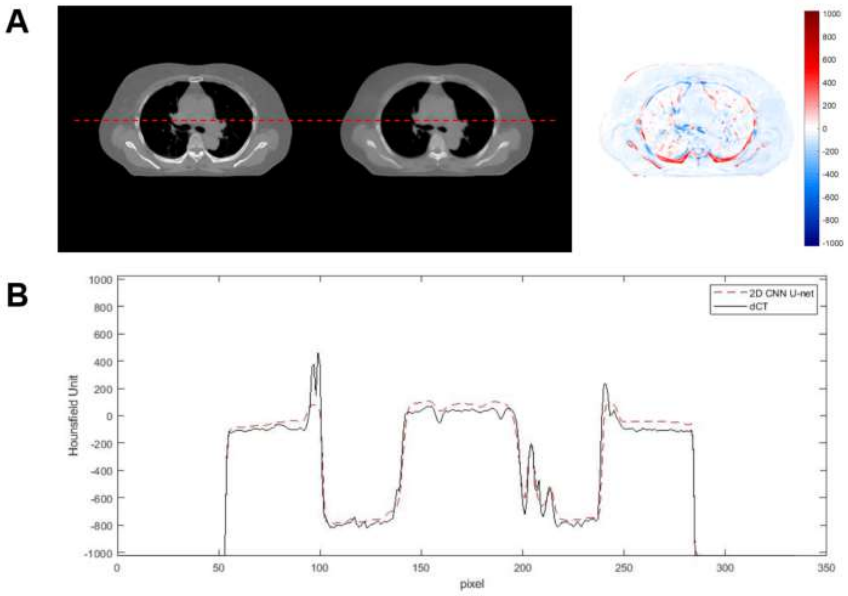

Figure 3-10. (A)The difference map between 2D CNN model sCT image and the dCT image for thorax, (B) The voxel-based HU profile of sCT(dash line) and dCT (solid line)

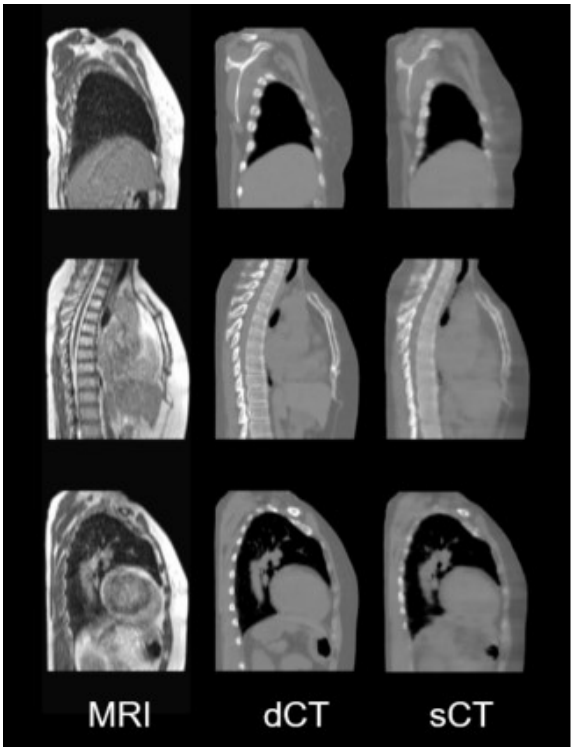

Figure 3-11. The representative sagittal slice views of MRI, dCT and sCT for thorax

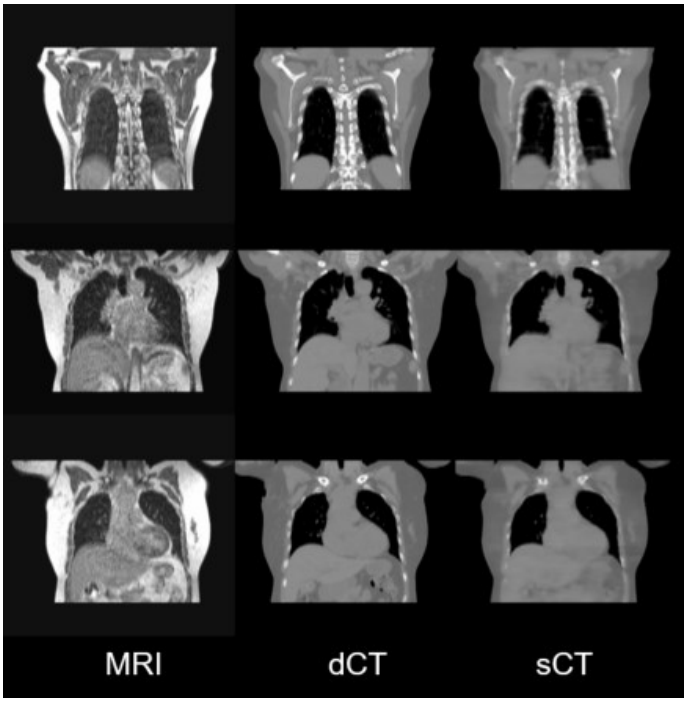

Figure 3-12. The representative coronal slice views of MRI, dCT and sCT for thorax

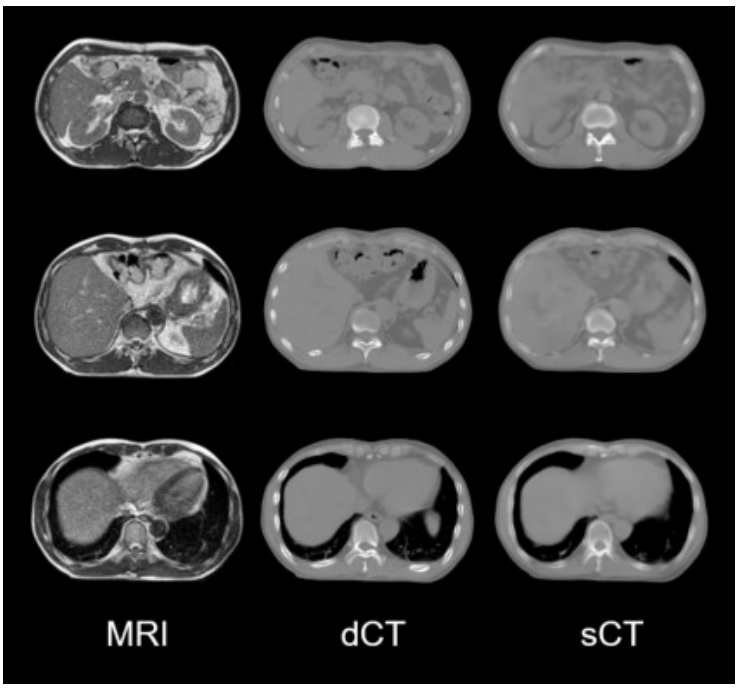

Figure 3-13. The representative axial slice views of MRI, dCT and sCT for abdomen

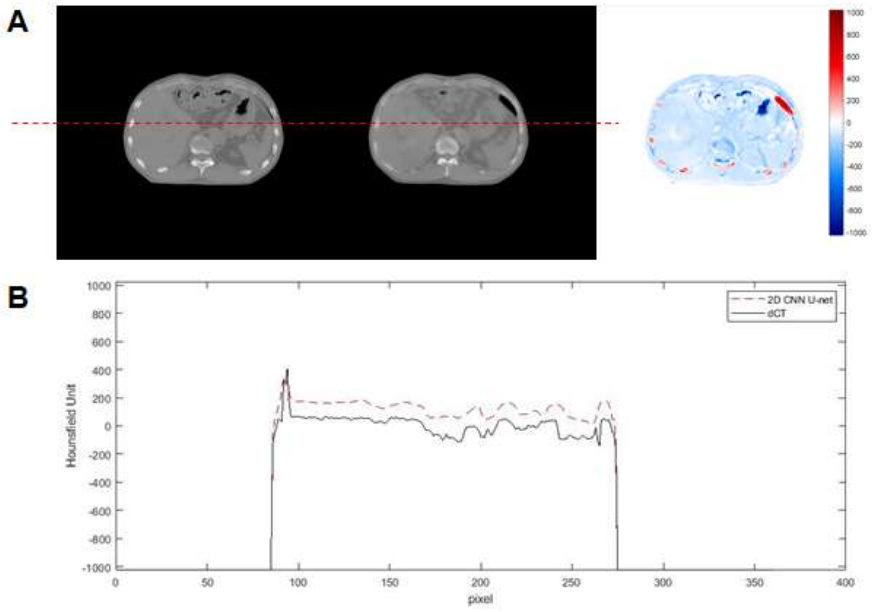

Figure 3-14. (A)The difference map between 2D CNN model sCT image and the dCT image for abdoemn, (B) The voxel-based HU profile of sCT(dash line) and dCT (solid line)

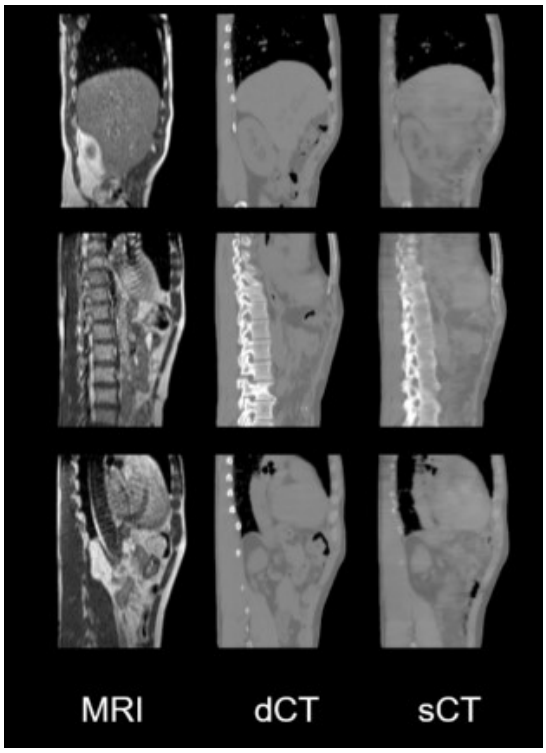

Figure 3-15. The representative sagittal slice views of MRI, dCT and sCT for abdomen

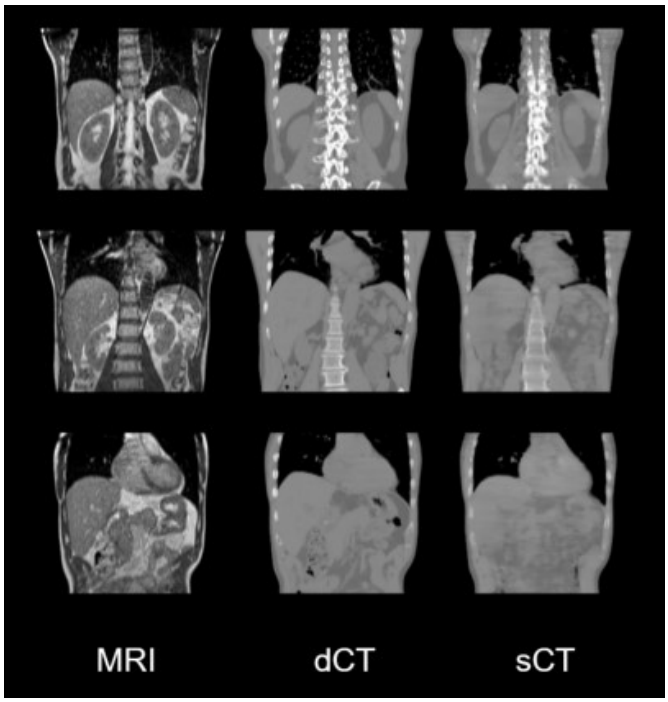

Figure 3-16. The representative coronal slice views of MRI, dCT and sCT for abdomen

3.3.2 Geomtric Analysis

For the 6 patients validation dataset in each region, MAE, RMSE, PSNR, and SSIM were computed using the equations from 3.2 to 3.5. The Table 3-2 summarized the results of geometric parameters. Comparing the average values of MAE, RMSE, and PSNR, the values in pelvic region show better acuuracy than the other two region. For instance considering the MAE values, the error gradually increases in the order of pelvis, thorax, abdomen with 44.02 ± 4.81, 66.36 ± 9.34, and 100.14 ± 36.80, respectively. On the other hand, SSIM showed contradictory results.

Table 3-2. Geometric comparison between dCT and sCT with respect to abdomen, thorax, and pelvis

Index	Pelvis	Thorax	Abdomen
MAE (HU)	44.02 ± 4.81	66.36 ± 9.34	100.14 ± 36.80
RMSE (HU)	94.26 ± 6.03	108.67 ± 10.30	132.84 ± 32.40
PSNR (dB)	28.73 ± 0.57	26.73 ± 0.70	25.11 ± 1.85
SSIM	0.88 ± 0.04	0.87 ± 0.02	0.92 ± 0.01

3.3.3 Dosimetric Analysis

Dose volume histogram (DVH) curves for PTV and relevant OARs in the pelvis, thorax, and abdomen are shown in Figure 3-17 A, B, and C, respectively. Figure 3-17 D, E, and F are enlarged views of each PTV curve. On the graph, the dotted line indicated the dCT and the solid line indicated the sCT. It showed that the dose distribution of sCT is nearly identical to that of dCT in most structures except the PTV in the abdominal region.

For quantitave analysis, clinically relevant DVH metrics were compared. The

mimimum, maximum, and mean value of absolute dose, and percent difference values between dCT and sCT in PTV were summarized in Figure 3-18. Comparison of all of DVH metrics between dCT and sCT for pelvis, thorax, and abdomen were summarized in Table 3-3, 3-4, and 3-5, respectively. The absolute value of PTV does not differ significantly between dCT and sCT in all three regions. However, it shoewed that dose overestimation of the sCT in PTV about 2% due to the percentage difference in Figure 3-18B.

Differences in OARs dose-volume metrics for each region are presented by box plots in Figures 3-19. Tables 3-6, 3-7, and 3-8 showed the average results of validation dataset DVH metrics corresponding to the different OARs. Since the *p*-values for all metrics are greater than 0.05, there was no significant difference in the OARs comparison.

The dCT-based and sCT-based dose ditribition were compared using gamma anaylsis. The Table 3-9 summarized gamma analysis of dose distributions with three different dose difference/distance-to agreement criteria : 1 mm/1%, 2 mm/2% and 3 mm/3%. Considering the 2 mm/2% criterion with a 10% low dose threshold, it showed all regions pass rate were above 97 %. If the gamma criterion is changed to 1 mm/1%, the overall gamma passing rate dcrease, especially in the abdolmen from 97.12 ± 2.00 to 78.50 ± 7.23. These trend is well llustrated in Figure 3-2 by gamma passing rates under 1 mm/1% and 2 mm/2% criterion.

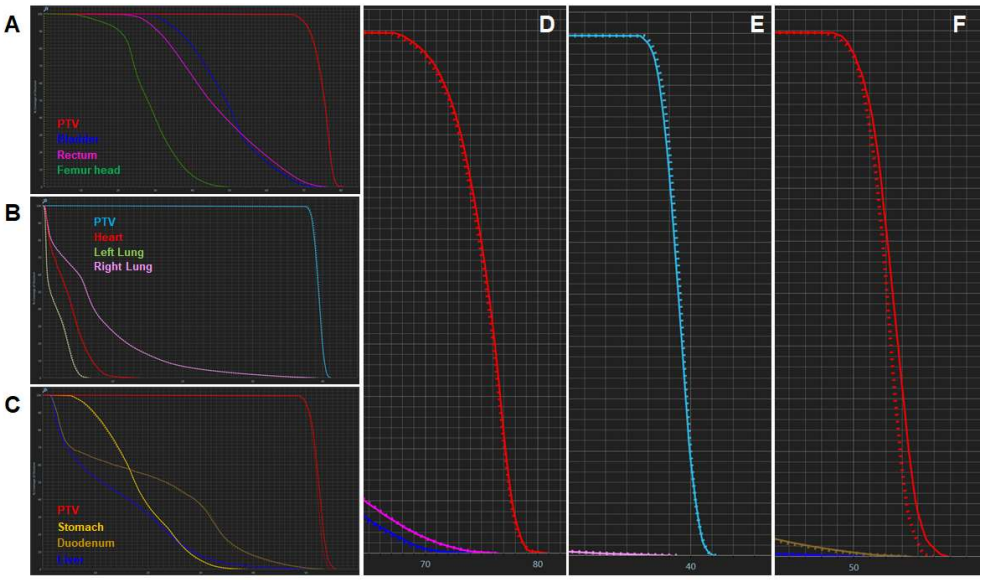

Figure 3-17. DVH curves for the PTV and OARs for (A) pelvis, (B) thorax, (C) abdomen, enlarged PTV graph in (D) to (F).
*DVH : Dose-volume histogram, Dotted line : dCT, Solide line : sCT

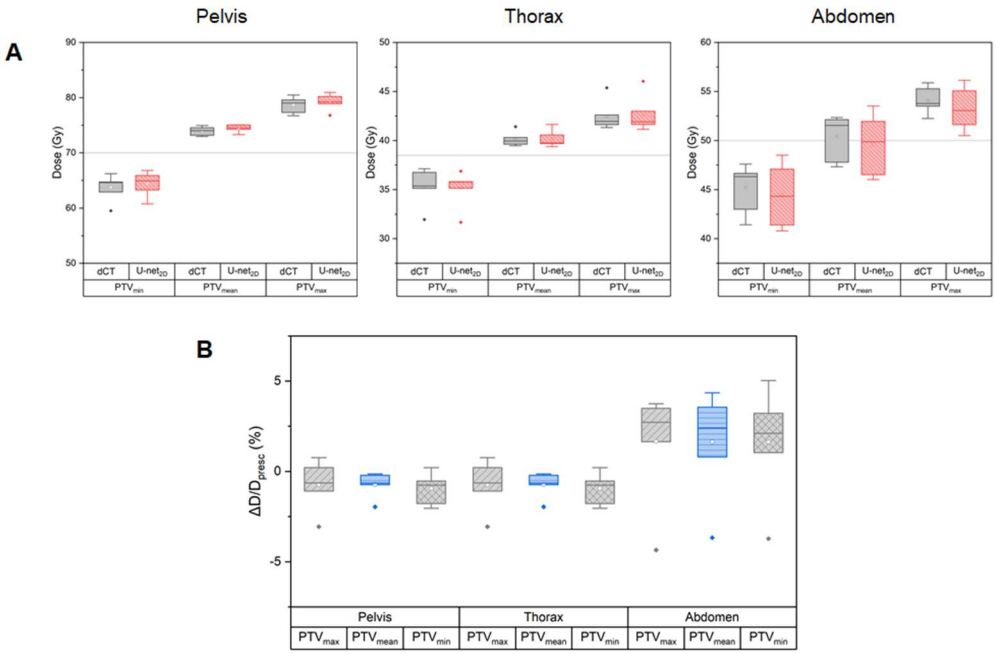

Figure 3-18. Box-plot of (A) absolute dose and (B) percent difference in PTV for each region. The maximum (top line), 75% (top of box), median (central point), 25% (bottom of box), and minimum (bottom line) are shown. Outliers are drawn as points.

Table 3-3. Dose-volume metrics of the PTV for pelvis

DV metric	dCT	sCT	*p-value*
PTV volume (cc)	81.09 ± 19.77		-
Maximum dose (Gy)	78.70 ± 1.31	79.22 ± 1.29	*0.229*
Mean dose (Gy)	73.94 ± 0.72	74.44 ± 0.62	*0.042*
Minimum dose (Gy)	63.77 ± 2.13	64.42 ± 1.97	*0.040*
$D_{98\%}$ (Gy)	68.58 ± 1.04	68.89 ± 0.98	*0.222*
$D_{2\%}$ (Gy)	76.94 ± 1.11	77.34 ± 0.96	*0.081*
$V_{100\%}$ (cc)	77.54 ± 18.82	78.52 ± 19.04	*0.035*
Homogeneity index	0.11 ± 0.02	0.11 ± 0.02	-
Conformity index	0.96 ± 0.01	0.97 ± 0.01	-

Table 3-4. Dose-volume metrics of the PTV for thorax

DV metric	dCT	sCT	*p-value*
PTV volume (cc)	95.37 ± 29.80		-
Maximum dose (Gy)	42.48± 1.36	42.61± 1.64	*0.400*
Mean dose (Gy)	40.13 ± 0.64	40.14± 0.77	*0.911*
Minimum dose (Gy)	35.28 ± 1.67	35.18 ± 1.65	*0.645*
$D_{98\%}$ (Gy)	37.67 ± 0.87	37.57± 0.72	*0.208*
$D_{2\%}$ (Gy)	41.85 ± 1.32	41.92± 1.44	*0.517*
$V_{100\%}$ (cc)	89.63 ± 27.79	88.11± 27.34	*0.070*
Homogeneity index	0.10 ± 0.05	0.11 ± 0.05	-
Conformity index	0.94 ± 0.01	0.92 ± 0.02	-

Table 3-5. Dose-volume metrics of the PTV for abdomen

DV metric	dCT	sCT	*p-value*
PTV volume (cc)	38.27 ± 13.64		-
Maximum dose (Gy)	54.08 ± 1.20	53.25 ± 1.93	*0.242*
Mean dose (Gy)	50.45 ± 2.07	49.63 ± 2.72	*0.225*
Minimum dose (Gy)	45.22 ± 2.22	44.41 ± 2.79	*0.239*
$D_{98\%}$ (Gy)	49.29 ± 0.16	48.57 ± 1.41	*0.276*
$D_{2\%}$ (Gy)	53.49 ± 0.58	52.90 ± 1.75	*0.448*
$V_{100\%}$ (cc)	36.10 ± 14.19	34.09 ± 16.61	*0.224*
Homogeneity index	0.08 ± 0.01	0.09 ± 0.01	-
Conformity index	0.94 ± 0.01	0.73 ± 0.029	-

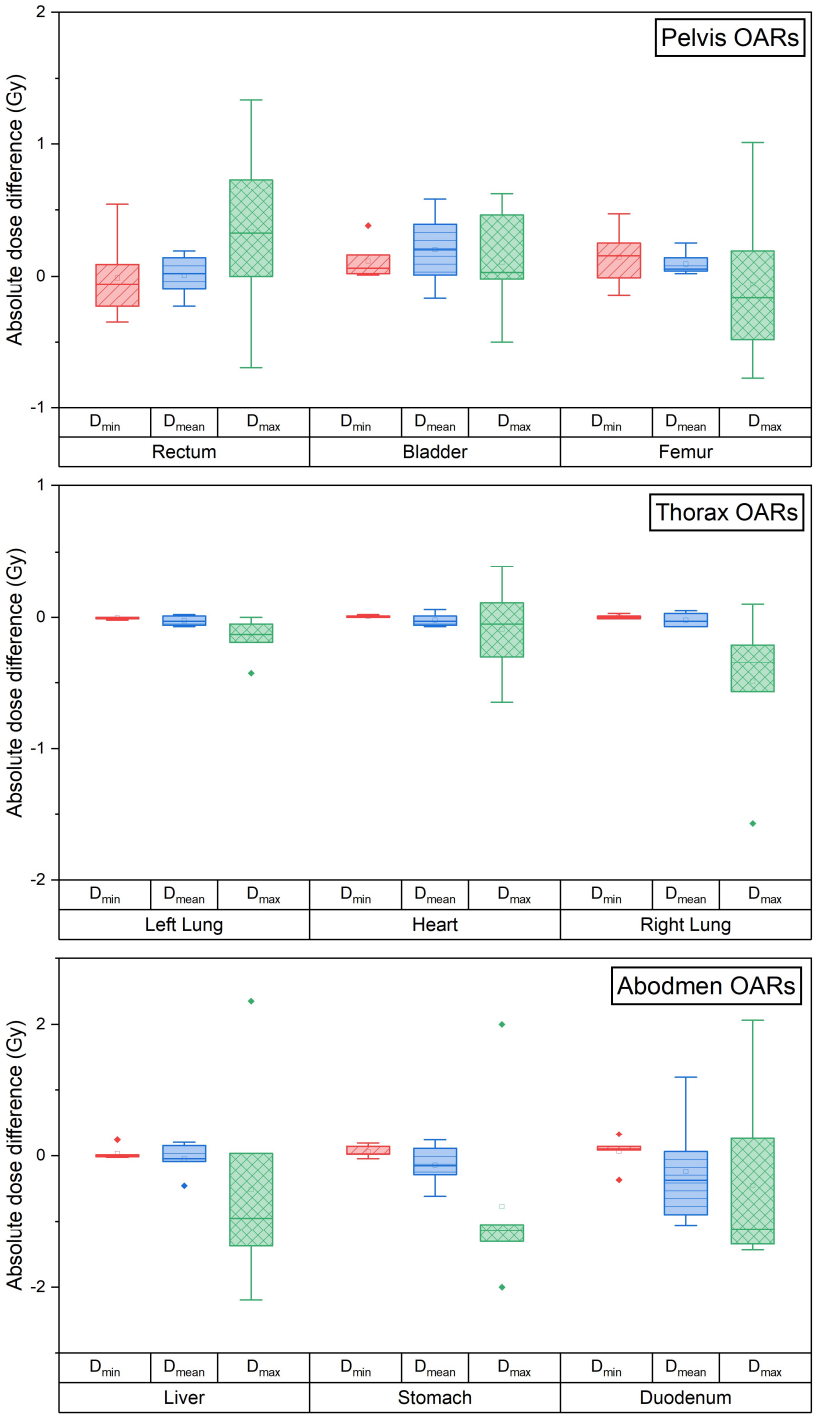

Figure 3-19. Box-plot of absolute dose difference between dCT and sCT in OARs for each region. The maximum (top line), 75% (top of box), median (central point), 25% (bottom of box), and minimum (bottom line) are shown. Outliers are drawn as points.

Table 3-6. Dose-volume metrics of the OARs for pelvis

DV metric	dCT	sCT	*p-value*
Bladder			
Maximum dose (Gy)	75.77 ± 1.55	75.87 ± 1.37	*0.551*
Mean dose (Gy)	47.30 ± 3.65	47.51 ± 3.60	*0.136*
Minimum dose (Gy)	20.01 ± 10.49	20.13 ± 10.50	*0.105*
Rectum			
Maximum dose (Gy)	76.07 ± 1.72	43.24 ± 6.12	*0.645*
Mean dose (Gy)	43.22 ± 6.14	43.24 ± 6.12	*0.600*
Minimum dose (Gy)	16.61 ± 8.01	16.53 ± 7.95	*0.291*
Femur head			
Maximum dose (Gy)	78.70 ± 1.31	79.22 ± 1.29	*0.904*
Mean dose (Gy)	73.94 ± 0.72	74.44 ± 0.62	*0.068*
Minimum dose (Gy)	63.77 ± 2.13	64.42 ± 1.97	*0.167*

Table 3-7. Dose-volume metrics of the OARs for thorax

DV metric	dCT	sCT	*p-value*
Heart			
Maximum dose (Gy)	19.01± 10.87	19.77 ± 9.95	*0.398*
Mean dose (Gy)	3.05 ± 0.73	2.92 ± 0.73	*0.327*
Minimum dose (Gy)	0.28 ± 0.09	0.28 ± 0.09	*0.856*
Left Lung			
Maximum dose (Gy)	9.05 ± 4.92	9.11 ± 4.84	*0.798*
Mean dose (Gy)	1.57 ± 0.31	1.66 ± 0.32	*0.472*
Minimum dose (Gy)	0.15 ± 0.03	0.16 ± 0.03	*0.447*
Right Lung			
Maximum dose (Gy)	40.09 ± 1.05	39.39 ± 1.05	*0.084*
Mean dose (Gy)	6.36 ± 1.36	6.64 ± 1.39	*0.389*
Minimum dose (Gy)	0.23 ± 0.08	0.26 ± 0.08	*0.289*

Table 3-8. Dose-volume metrics of the OARs for abdomen

DV metric	dCT	sCT	*p-value*
Duodenum			
Maximum dose (Gy)	26.14 ± 8.89	25.89 ± 9.11	*0.462*
Mean dose (Gy)	26.14 ± 8.89	25.89 ± 9.11	*0.495*
Minimum dose (Gy)	5.35 ± 5.12	5.41± 5.00	*0.532*
Liver			
Maximum dose (Gy)	44.46 ± 8.85	43.94 ± 9.52	*0.233*
Mean dose (Gy)	8.32 ± 5.26	8.27 ± 5.19	*0.291*
Minimum dose (Gy)	0.73 ± 0.33	0.76 ± 0.39	*0.170*
Stomach			
Maximum dose (Gy)	45.45 ± 5.19	44.67 ± 5.75	*0.459*
Mean dose (Gy)	15.23 ± 5.09	15.09 ± 5.00	*0.608*
Minimum dose (Gy)	2.10 ± 1.63	2.16 ± 1.71	*0.485*

Table 3-9. Gamma analysis results comparing the dCT-based plan with sCT-based plan

Gamma criterion	Dose > 10%	Dose > 50%	Dose > 90%
Pelvis			
1mm / 1%	87.63 ± 6.86	73.92 ± 17.75	63.25 ± 21.60
2mm / 2%	98.45 ± 0.95	98.01 ± 2.50	93.26 ± 10.42
3mm / 3%	99.32 ± 0.68	99.70 ± 0.48	98.96 ± 2.17
Thorax			
1mm / 1%	91.14 ± 1.25	69.07 ± 3.33	64.28 ± 4.00
2mm / 2%	99.74 ± 0.07	98.36 ± 0.51	96.06 ± 1.43
3mm / 3%	99.99 ± 0.01	99.94 ± 0.07	99.85 ± 0.15
Abdomen			
1mm / 1%	78.50 ± 7.23	28.83 ± 17.61	16.40 ± 17.56
2mm / 2%	97.12 ± 2.00	81.15± 11.73	40.52 ± 30.93
3mm / 3%	99.09 ± 0.83	93.57± 5.90	70.20 ± 24.13

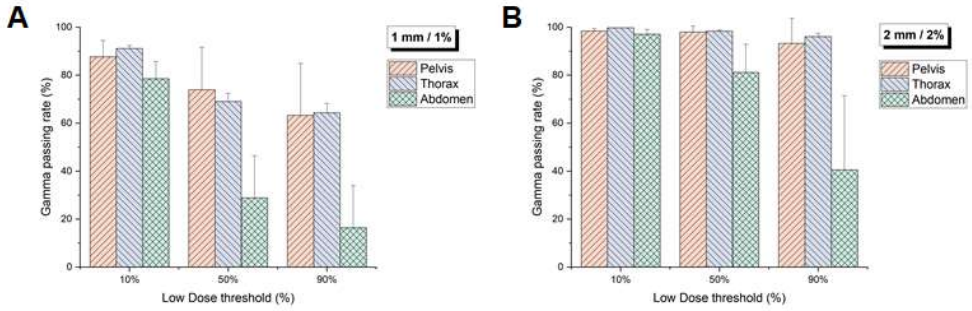

Figure 3-20. Bargraph of Gamma passing rate for each region (A) 1 mm/1% (B) 2mm/2% criterion.

3.4. Discussion

MR-IGRT with daily adaptive treatment enables to observe tumor reduction in real-time. This allows intensive treatment on the remaining tumors while minimizing exposure to the surrounding organs. If the tumor size dramatically changes during radiotherapy, adaptive MR-IGRT can be used to further reduce normal tissue dose, eventually reduce decrease adverse events. Several studies and clinical trials have reported promising results in terms of tumour control, toxicity occurrence and survival rates using MR-IGRT in breast and pancreatic caner (54-56). In this regard, MR-IGRT is the latest treatment technology capable of verification of volumetric dose distribution in real time. However, the deformation registration algorithm commonly used in MR-IGRT is limited in accuracy, which may lead to inaccurate calculation of dose distribution. Therefore, generating synthetic CT from MR images acquired in real time is the an alternative way to calculate more accurate dose distribution.

In this study, we applied and assessed 2D CNN U-net model to generate sCT for MR-IGRT dose calculation. The 2D CNN U-net model was chosen as a deep

learning method due to much less time-consuming and high accuracy compared to the atlas or segmentation based synthetic CT generation method. The difference from previously reported studies is that the proposed 2D CNN U-net network is applied and compared to three different areas of the pelvis, thorax, and abdomen simutaneously.

To quantiatatively evaluate the quality of the sCT, geometrical analysis and dosimetric end analysis were performed. The results demonstrated highly accurate and efficient performance in sCT generation. Most of *p* values in PTV and OARs were greater than 0.05, indicating no significant diffrence in dose metrics between the dCT and sCT. However, there was a difference in accuracy depending on the dataset region. The pelvis and thorax data showed that dCT and sCT were almost similar in all the indicators, but the abdomen showed an inferior accuracy compared to the two regions. This is due to the degree of mismatch in deformed registration bewteen MR and CT. The 2D CNN U-net model valid only when the MR and CT images are perfectly registred. It is not feasible given the mismatch between MR and CT images by organ motion or air poecket that easily observed in the abdominal region. Therefore, using the cycleGAN trained with unpaired samples would have a potential improvement on dosimetric accuracy (57-59).

The dose accuracy of sCT could be predicted through geometric analysis values obtained from inter-voxel results of predicted HU values. MAE, RMSE, and PSNR all showed high accuracy in the order of pelvis, thorax, and abdomen, which showed the same trend in DV metric and gamma analysis. However, since SSIM considered all luminance, contrast, and structural characteristics between images, it was difficult to find a problem caused by a difference in HU values. Therefore, contrary to the previous results, it showed similarity in the order of the abdomen, thorax, and pelvis.

From the image comparison results, HU estimation of bony stsuctures were not sufficiently represented on the sCT. One possible reason could be the large interpatient variability of CT intensity distribution within bony structure (34). To solve this problem, adding additional anatomical information in the training data for the 2D CNN U-net could further improve the CT number estimation accuracy. In the process of radiotherpay, it was requried contouring of tumor and normal organs. Therefore, in preparing the data set, additional contouring of the air pocket and the bone can improve accuracy.

Chapter 4. Conclusions

We have developed an UTE MR-AC method using level-set segmentation with inhomogeneity correction for brain PET/MRI studies, and demonstrated the feasibility of this method in brain PET/MRI studies with [^{18}F]FP-CIT and [^{18}F]FDG. The MR-based attenuation maps generated using level-set segmentation and PET images corrected for attenuation and scatter using it was superior to those offered by the manufacturer of the PET/MRI system in terms of the similarity to the CT-AC. This method will be useful for improving the quantitative accuracy of brain PET in PET/MRI studies.

We have applied 2D CNN U-net network and evaluated the low field MR-based sCT compared to dCT. It can generate accurate sCT images from low field MR images fully automatic within seconds. Compared with dCT generated by deformed registration, the sCT provided low dose uncerttainties by DVH metric and gamma analysis. Therefore, the proposed method clinically acceptable for MR-IGRT planning. It suggests the possibility of MR-only radiation therapy framework.

Bibliography

1. Schlemmer HP, Pichler BJ, Schmand M, Burbar Z, Michel C, Ladebeck R, et al. Simultaneous MR/PET imaging of the human brain: feasibility study. Radiology. 2008;248(3):1028-35.
2. Catana C, Wu Y, Judenhofer MS, Qi J, Pichler BJ, Cherry SR. Simultaneous acquisition of multislice PET and MR images: initial results with a MR-compatible PET scanner. J Nucl Med. 2006;47(12):1968-76.
3. Pichler BJ, Judenhofer MS, Catana C, Walton JH, Kneilling M, Nutt RE, et al. Performance test of an LSO-APD detector in a 7-T MRI scanner for simultaneous PET/MRI. J Nucl Med. 2006;47(4):639-47.
4. Yoon HS, Ko GB, Kwon SI, Lee CM, Ito M, Chan Song I, et al. Initial results of simultaneous PET/MRI experiments with an MRI-compatible silicon photomultiplier PET scanner. J Nucl Med. 2012;53(4):608-14.
5. Yamamoto S, Watabe T, Watabe H, Aoki M, Sugiyama E, Imaizumi M, et al. Simultaneous imaging using Si-PM-based PET and MRI for development of an integrated PET/MRI system. Phys Med Biol. 2012;57(2):N1-13.
6. Catana C, Drzezga A, Heiss WD, Rosen BR. PET/MRI for neurologic applications. J Nucl Med. 2012;53(12):1916-25.
7. Jaffray DA. Image-guided radiotherapy: from current concept to future perspectives. Nat Rev Clin Oncol. 2012;9(12):688-99.
8. Goyal S, Kataria T. Image guidance in radiation therapy: techniques and applications. Radiol Res Pract. 2014;2014:705604.
9. Hartford AC, Palisca MG, Eichler TJ, Beyer DC, Devineni VR, Ibbott GS, et al. American Society for Therapeutic Radiology and Oncology (ASTRO) and American College of Radiology (ACR) Practice Guidelines for Intensity-Modulated Radiation Therapy (IMRT). Int J Radiat Oncol Biol Phys. 2009;73(1):9-14.
10. Guckenberger M, Andratschke N, Alheit H, Holy R, Moustakis C, Nestle U, et al. Definition of stereotactic body radiotherapy: principles and practice for the treatment of stage I non-small cell lung cancer. Strahlenther Onkol. 2014;190(1):26-33.
11. Boda-Heggemann J, Lohr F, Wenz F, Flentje M, Guckenberger M. kV cone-beam CT-based IGRT: a clinical review. Strahlenther Onkol. 2011;187(5):284-91.
12. Martins L, Couto JG, Barbosa B. Use of planar kV vs. CBCT in evaluation of setup errors in oesophagus carcinoma radiotherapy. Rep Pract Oncol Radiother. 2016;21(1):57-62.
13. Mutic S, Dempsey JF. The ViewRay system: magnetic resonance-guided and controlled radiotherapy. Semin Radiat Oncol. 2014;24(3):196-9.
14. Henke LE, Contreras JA, Green OL, Cai B, Kim H, Roach MC, et al. Magnetic Resonance Image-Guided Radiotherapy (MRIgRT): A 4.5-Year Clinical Experience. Clin Oncol (R Coll Radiol). 2018;30(11):720-7.
15. Hu Y, Rankine L, Green OL, Kashani R, Li HH, Li H, et al. Characterization of the onboard imaging unit for the first clinical magnetic resonance image guided radiation therapy system. Med Phys. 2015;42(10):5828-37.
16. Kim JI, Lee H, Wu HG, Chie EK, Kang HC, Park JM. Development of patient-controlled respiratory gating system based on visual guidance for magnetic-resonance image-guided radiation therapy. Med Phys. 2017;44(9):4838-46.
17. Green OL, Rankine LJ, Cai B, Curcuru A, Kashani R, Rodriguez V, et al. First clinical implementation of real-time, real anatomy tracking and radiation beam control. Med Phys. 2018.
18. Carney JP, Townsend DW, Rappoport V, Bendriem B. Method for transforming CT images for attenuation correction in PET/CT imaging. Med Phys. 2006;33(4):976-83.
19. Kinahan PE, Hasegawa BH, Beyer T. X-ray-based attenuation correction for positron emission tomography/computed tomography scanners. Semin Nucl Med. 2003;33(3):166-79.

20. Saw CB, Loper A, Komanduri K, Combine T, Huq S, Scicutella C. Determination of CT-to-density conversion relationship for image-based treatment planning systems. Med Dosim. 2005;30(3):145-8.
21. Ahnesjo A, Andreo P, Brahme A. Calculation and application of point spread functions for treatment planning with high energy photon beams. Acta Oncol. 1987;26(1):49-56.
22. Keereman V, Mollet P, Berker Y, Schulz V, Vandenberghe S. Challenges and current methods for attenuation correction in PET/MR. MAGMA. 2013;26(1):81-98.
23. Wagenknecht G, Kaiser HJ, Mottaghy FM, Herzog H. MRI for attenuation correction in PET: methods and challenges. MAGMA. 2013;26(1):99-113.
24. Edmund JM, Nyholm T. A review of substitute CT generation for MRI-only radiation therapy. Radiat Oncol. 2017;12(1):28.
25. Kops ER, Herzog H, Shah NJ. Comparison template-based with CT-based attenuation correction for hybrid MR/PET scanners. EJNMMI Phys. 2014;1(Suppl 1):A47.
26. Montandon ML, Zaidi H. Atlas-guided non-uniform attenuation correction in cerebral 3D PET imaging. Neuroimage. 2005;25(1):278-86.
27. Andreasen D, Van Leemput K, Edmund JM. A patch-based pseudo-CT approach for MRI-only radiotherapy in the pelvis. Med Phys. 2016;43(8):4742.
28. Sjolund J, Forsberg D, Andersson M, Knutsson H. Generating patient specific pseudo-CT of the head from MR using atlas-based regression. Phys Med Biol. 2015;60(2):825-39.
29. Uh J, Merchant TE, Li Y, Li X, Hua C. MRI-based treatment planning with pseudo CT generated through atlas registration. Med Phys. 2014;41(5):051711.
30. Leynes AP, Yang J, Shanbhag DD, Kaushik SS, Seo Y, Hope TA, et al. Hybrid ZTE/Dixon MR-based attenuation correction for quantitative uptake estimation of pelvic lesions in PET/MRI. Med Phys. 2017;44(3):902-13.
31. Delso G, Wiesinger F, Sacolick LI, Kaushik SS, Shanbhag DD, Hullner M, et al. Clinical evaluation of zero-echo-time MR imaging for the segmentation of the skull. J Nucl Med. 2015;56(3):417-22.
32. Han X. MR-based synthetic CT generation using a deep convolutional neural network method. Med Phys. 2017;44(4):1408-19.
33. Nie D, Trullo R, Lian J, Petitjean C, Ruan S, Wang Q, et al. Medical Image Synthesis with Context-Aware Generative Adversarial Networks. Med Image Comput Comput Assist Interv. 2017;10435:417-25.
34. Chen S, Qin A, Zhou D, Yan D. Technical Note: U-net-generated synthetic CT images for magnetic resonance imaging-only prostate intensity-modulated radiation therapy treatment planning. Med Phys. 2018;45(12):5659-65.
35. Dinkla AM, Wolterink JM, Maspero M, Savenije MHF, Verhoeff JJC, Seravalli E, et al. MR-Only Brain Radiation Therapy: Dosimetric Evaluation of Synthetic CTs Generated by a Dilated Convolutional Neural Network. Int J Radiat Oncol Biol Phys. 2018;102(4):801-12.
36. Maspero M, Savenije MHF, Dinkla AM, Seevinck PR, Intven MPW, Jurgenliemk-Schulz IM, et al. Dose evaluation of fast synthetic-CT generation using a generative adversarial network for general pelvis MR-only radiotherapy. Phys Med Biol. 2018;63(18):185001.
37. Lundervold AS, Lundervold A. An overview of deep learning in medical imaging focusing on MRI. Z Med Phys. 2019;29(2):102-27.
38. Christen T, Sheikine Y, Rocha VZ, Hurwitz S, Goldfine AB, Di Carli M, et al. Increased glucose uptake in visceral versus subcutaneous adipose tissue revealed by PET imaging. JACC Cardiovasc Imaging. 2010;3(8):843-51.
39. Dickson JC, O'Meara C, Barnes A. A comparison of CT- and MR-based attenuation correction in neurological PET. Eur J Nucl Med Mol Imaging. 2014;41(6):1176-89.
40. Keereman V, Fierens Y, Broux T, De Deene Y, Lonneux M, Vandenberghe S. MRI-based attenuation correction for PET/MRI using ultrashort echo time sequences. J Nucl Med.

2010;51(5):812-8.
41. Catana C, van der Kouwe A, Benner T, Michel CJ, Hamm M, Fenchel M, et al. Toward implementing an MRI-based PET attenuation-correction method for neurologic studies on the MR-PET brain prototype. J Nucl Med. 2010;51(9):1431-8.
42. Cabello J, Lukas M, Forster S, Pyka T, Nekolla SG, Ziegler SI. MR-based attenuation correction using ultrashort-echo-time pulse sequences in dementia patients. J Nucl Med. 2015;56(3):423-9.
43. Choi H, Cheon GJ, Kim HJ, Choi SH, Lee JS, Kim YI, et al. Segmentation-based MR attenuation correction including bones also affects quantitation in brain studies: an initial result of 18F-FP-CIT PET/MR for patients with parkinsonism. J Nucl Med. 2014;55(10):1617-22.
44. Chan TF, Vese LA. Active contours without edges. Ieee T Image Process. 2001;10(2):266-77.
45. Vese LA, Chan TF. A multiphase level set framework for image segmentation using the Mumford and Shah model. Int J Comput Vision. 2002;50(3):271-93.
46. Li C, Huang R, Ding Z, Gatenby JC, Metaxas DN, Gore JC. A level set method for image segmentation in the presence of intensity inhomogeneities with application to MRI. IEEE Trans Image Process. 2011;20(7):2007-16.
47. Park JM, Park SY, Kim HJ, Wu HG, Carlson J, Kim JI. A comparative planning study for lung SABR between tri-Co-60 magnetic resonance image guided radiation therapy system and volumetric modulated arc therapy. Radiother Oncol. 2016;120(2):279-85.
48. Largent A, Barateau A, Nunes JC, Lafond C, Greer PB, Dowling JA, et al. Pseudo-CT Generation for MRI-Only Radiation Therapy Treatment Planning: Comparison Among Patch-Based, Atlas-Based, and Bulk Density Methods. Int J Radiat Oncol Biol Phys. 2019;103(2):479-90.
49. Fu J, Yang Y, Singhrao K, Ruan D, Chu FI, Low DA, et al. Deep learning approaches using 2D and 3D convolutional neural networks for generating male pelvic synthetic computed tomography from magnetic resonance imaging. Med Phys. 2019;46(9):3788-98.
50. Largent A, Barateau A, Nunes JC, Mylona E, Castelli J, Lafond C, et al. Comparison of Deep Learning-Based and Patch-Based Methods for Pseudo-CT Generation in MRI-Based Prostate Dose Planning. Int J Radiat Oncol Biol Phys. 2019;105(5):1137-50.
51. Tustison NJ, Avants BB, Cook PA, Zheng Y, Egan A, Yushkevich PA, et al. N4ITK: improved N3 bias correction. IEEE Trans Med Imaging. 2010;29(6):1310-20.
52. Olaf Ronneberger PF, Thomas Brox. U-Net: Convolutional Networks for Biomedical Image Segmentation. arXiv.
53. Low DA, Harms WB, Mutic S, Purdy JA. A technique for the quantitative evaluation of dose distributions. Med Phys. 1998;25(5):656-61.
54. Jeon SH, Shin KH, Park SY, Kim JI, Park JM, Kim JH, et al. Seroma change during magnetic resonance imaging-guided partial breast irradiation and its clinical implications. Radiat Oncol. 2017;12(1):103.
55. Mittauer K, Paliwal B, Hill P, Bayouth JE, Geurts MW, Baschnagel AM, et al. A New Era of Image Guidance with Magnetic Resonance-guided Radiation Therapy for Abdominal and Thoracic Malignancies. Cureus. 2018;10(4):e2422.
56. Boldrini L, Cusumano D, Cellini F, Azario L, Mattiucci GC, Valentini V. Online adaptive magnetic resonance guided radiotherapy for pancreatic cancer: state of the art, pearls and pitfalls. Radiat Oncol. 2019;14(1):71.
57. Zhu J Y PT, Isola P, Efros A A. Unpaired Image-to-Image Translation using Cycle-Consistent Adversarial Networks. IEEE International Conference on Computer Vision. 2017.
58. Klages P, Benslimane I, Riyahi S, Jiang J, Hunt M, Deasy JO, et al. Patch-based generative adversarial neural network models for head and neck MR-only planning. Med Phys. 2020;47(2):626-42.
59. Dong X, Lei Y, Tian S, Wang T, Patel P, Curran WJ, et al. Synthetic MRI-aided

multi-organ segmentation on male pelvic CT using cycle consistent deep attention network. Radiother Oncol. 2019;141:192-9.

Abstract in Korean (국문 초록)

지난 10년간 진단 및 치료분야에서 자기공명영상(Magnetic resonance imaging; MRI) 의 적용이 증가하였다. MRI는 CT와 비교해 추가적인 전리방사선의 피폭없이 뇌, 복부 기관 및 골수 등에서 더 높은 연조직 대비를 제공한다. 따라서 MRI를 적용한 양전자방출단층촬영(Positron emission tomography; PET)/MR 시스템과 MR 영상 유도 방사선 치료 시스템(MR-image guided radiation therapy; MR-IGRT)이 진단 및 치료 방사선분야에 등장하여 임상에 사용되고 있다.

PET/MR 시스템의 한 가지 주요 문제는 PET 정량화를 위한 MRI 스캔으로부터의 감쇠 보정이며, MR-IGRT 시스템에서 선량 계산을 위해 MR 영상에 전자 밀도를 할당하는 것과 비슷한 필요성을 찾을 수 있다. 이는 MR 신호가 전자 밀도가 아닌 조직의 양성자 밀도 및 T1, T2 이완 특성과 관련이 있기 때문이다. 이 문제를 극복하기 위해, MR 이미지로부터 유래된 가상의 CT인 합성 CT라 불리는 방법이 제안되었다. 본 학위논문에서는 합성 CT 생성 방법 및 진단 및 방사선 치료에 적용을 위한 MR 영상 기반 합성 CT 사용의 임상적 타당성을 조사하였다.

첫째로, 뇌 PET/MR를 위한 레벨셋 분할을 이용한 MR 이미지 기반 감쇠 보정 방법을 개발하였다. MR 이미지 기반 감쇠 보정의 부정확성은 정량화 오류와 뇌 PET/MRI 연구에서 병변의 잘못된 판독으로 이어진다. 이 문제를 해결하기 위해, 자기장 불균일 보정을 포함한 다상 레벨셋

알고리즘에 기초한 개선된 초단파 에코 시간 MR-AC 방법을 제안하였다. 또한 CT-AC 및 PET/MRI 스캐너 제조업체가 제공한 MR-AC와 비교하여 레벨셋 기반 MR-AC 방법의 임상적 사용가능성을 평가하였다.

둘째로, MR-IGRT 시스템을 위한 심층 컨볼루션 신경망 모델을 사용하여 저필드 MR 이미지에서 생성된 합성 CT 방법를 제안하였다. 이 합성 CT 이미지를 변형 정합을 사용하여 생성된 변형 CT와 비교하였다. 또한 골반, 흉부 및 복부 환자에서의 기하학적, 선량적 분석을 통해 방사선 치료계획에서의 합성 CT를 사용가능성을 평가하였다.

주요어 : 합성 CT, 가상 CT, PET/MRI, MR-IGRT, 감쇠보정, 전자 밀도 지도

학번 : 2012-30578